



Final Draft of the original manuscript

Deng, M.; Wang, L.; Höche, D.; Lamaka, S.; Snihirova, D.; Jiang, P.; Zheludkevich, M.:

Corrosion and discharge properties of Ca/Ge micro-alloyed Mg anodes for primary aqueous Mg batteries.

In: Corrosion Science. Vol. 177 (2020) 108958.

First published online by Elsevier: 20.08.2020

<https://dx.doi.org/10.1016/j.corsci.2020.108958>

Corrosion and discharge properties of Ca/Ge micro-alloyed Mg anodes for primary aqueous Mg batteries

Min Deng^{a,*}, Linqian Wang^{a,*}, Daniel Höche^a, Sviatlana V. Lamaka^a, Darya Snihirova^a, Pingli Jiang^a, Mikhail

L. Zheludkevich^{a,b}

^a MagIC – Magnesium Innovation Centre, Helmholtz-Zentrum Geesthacht (HZG), 21502 Geesthacht, Germany^b

Institute of Materials Science, Faculty of Engineering, Kiel University, 24143 Kiel, Germany

Abstract: Ge is evaluated as a micro-alloying element for newly-developed Mg-Ca anodes. The combination of Ca/Ge is effective for suppressing cathodic HER kinetics, resulting in highly negative OCP and a low corrosion rate (0.2 mm y^{-1}). For air battery, Mg-0.1%Ca-0.1%Ge (wt%) anode exhibits similar voltage to Mg-0.1%Ca in NaCl solution, but the highly negative OCP enables it with enhanced voltage in salicylate-containing electrolyte (1.7 V at 1 mA cm^{-2} versus 1.63 V of Mg-0.1%Ca). Beside, all micro-alloyed Mg-Ca, Mg-Ge and Mg-Ca-Ge anodes show similar self-discharge rates and high utilization efficiency ($\sim 60\%$ at 10 mA cm^{-2}).

Keywords: A. Magnesium; B. Galvanostatic; B. Polarization; B. Weight loss; C. Anodic dissolution.

1. Introduction

Primary batteries, which are non-rechargeable and designed to be used only once, are being utilized in numerous applications, like offshore equipment, implanted medical devices, and as standby power sources for schools, hospitals, etc., due to their long shelf-life, high energy density and instant readiness [1, 2]. Among all developed primary batteries, primary Mg system owns great promise attributed to the low cost of Mg raw materials and good theoretical electrochemical properties of Mg metal, e.g. the large volumetric capacity (3832 mA h g^{-1} versus 2061 mA h g^{-1} of Li) and highly negative electrode potential (-2.37 V vs. SHE) [3-6]. Primary Mg batteries can be designed as several types, e.g., Mg-air battery, Mg-seawater battery and Mg dry cell, via adopting different oxidizing agents, like oxygen from air, AgCl and MnO_2 [1, 7, 8]. The electrolyte used in primary Mg system is manmade nontoxic saline solution (often with additives) or natural ocean water [9-12]. The utilization of all nonhazardous components renders the Mg primary system an environmentally

benign power source meeting the social

* Corresponding author.

M. Deng: Min.Deng@hzg.de, Telephone number: +49 (0)4152 871936.

L. Wang: Linqian.Wang@hzg.de, Telephone number: +49 (0)4152 871906

demand for green energy. However, their commercialization is not widely fulfilled, especially the Mg-air batteries, being hindered by several issues weakening the practical properties. Concern on Mg anode derives from two main aspects. Firstly, copious hydrogen evolution takes place on Mg anode surface under anodic polarization in aqueous solutions. The hydrogen evolution rate increases with elevating anodic current (or anodic potential), leading to severe wasteful dissolution of Mg anode. This unusual phenomenon, which is termed as negative difference effect (NDE), leads to a shortened shelf life and reduced energy density of Mg-based battery system. Secondly, the battery voltage is relatively low comparing to the theoretical value because of the high open circuit potential (OCP) of ordinary Mg anode and large voltage drop caused by sluggish anodic reaction kinetics or dense discharge products film on anode surface [13-17]. In this context, the performance boost of Mg-based primary batteries requires more effort for development of Mg anodes with higher corrosion resistance, low self-discharge rate, low OCP (high cell voltage) and high discharge activity.

Increasing the purity grade of Mg could be an effective method to improve the properties of Mg anode. As reported, an Mg-air cell based on a high-purity Mg (99.99%) anode showed higher discharge voltage than the system with some commercial Mg alloy anodes, e.g. AM50 and AZ91 [18]. However, the corrosion and electrochemical performance of high purity Mg are dominated by the amount and composition of Fe-containing precipitates [19-22], which are uncontrollable during solidification process. It was proposed high purity Mg with minimal Fe-rich particles should have an intrinsic corrosion rate of $\sim 0.3 \text{ mm y}^{-1}$ in concentrated NaCl solution [23]. In contrast, with presence of Fe-rich precipitates, significantly higher corrosion rate and altered electrochemical properties are induced. The poor reproducibility of pure Mg properties, which is associated with metallurgic processing, results in its inadequacy as an anode material. Modification of pure Mg morphology also attracts some interests regarding anode developing. Further, Mg with varied nano/mesoscale structures has been evaluated as the anode material for Mg primary system, such as nanospheres, nanorods and porous thin film [24-28]. Enhancement on cell voltage was obtained due to increased contact with electrolyte and reduced charge transfer polarization. However, the usage of nanostructured Mg accelerated the anode self-corrosion, which reduced battery capacity and energy density and, therefore, lead to the request for electrolyte additives with capability of inhibiting self-corrosion. Another popular approach for Mg anode

development is alloying by other metallic elements with consequent composition optimization. Many Mg alloys have been proposed as anode materials for primary Mg batteries during the past decades [15, 17, 29-33], among which most are based on Mg-Al system as Al is the most commonly used alloying element for Mg to improve its corrosion resistance and mechanical properties. The improved corrosion resistance by Al alloying is believed to be associated with the formation of a protective film attributed to Al enrichment [34, 35]. However, at the same time, the protective film certainly results in large voltage drop during discharge and then leads to reduced battery voltage [36]. Moreover, as summarized, Mg-Al based alloys normally possess more positive OCP [17]. Therefore, novel Al-free Mg anodes with excellent performance are preferred. Importantly, our previous work indicates that binary Mg-Ca alloys possess great potential as environmentally benign anode materials with superior discharge properties [37, 38]. Mg-0.1 wt% Ca alloy showed higher discharge voltage and energy density than high purity Mg, AM50 and AZ31 alloys measured in a custom-made Mg-air full cell. Nevertheless, there is still space for improvement in what concerns the Mg-Ca anodes because the voltage and peak energy density were insufficient comparing to the theoretical values. Thus, further enhancement on Mg-Ca based anodes is desirable.

Improvement is possible by introducing electrolyte additives. For instance, by using Mg^{2+} complexing agents, like salicylate (SAL), the formation of surface $Mg(OH)_2$ film was impeded and thus the pure Mg- and Mg-Ca-based battery voltage was enhanced, particularly under low current densities [10, 39, 40]. The working condition needs to be optimized to obtain sufficiently high utilization efficiency along with enhanced voltage. Besides, alloying remains a worth-trying approach for the performance boosting of Mg-Ca anodes. However, the alloying elements should be carefully selected. Besides, the alloying content should be controlled within a relatively low level for purpose of reducing second phase fraction. Deng et al. [41] demonstrated that cathodic acting secondary phases with respect to Mg matrix will be detached from anode substrate during discharge process because of the preferential dissolution of surrounding Mg matrix. Besides, secondary phases and impurity particles may also lead to localized and non-uniform anodic dissolution, resulting in Mg matrix undermining and then peeling from substrate. The detachment of secondary phases and undermined matrix, which is named chunk effect (CE), leads to large anodic efficiency loss and consequently reduces battery service life and

energy density. Therefore, low alloyed Mg anodes are required to moderate the performance loss related to CE [42, 43]. Recently, published work demonstrated that germanium (Ge) as a trace alloying element is able to enhance the corrosion resistance of pure Mg (99.95%, corrosion rate of 20 mm y⁻¹ in 0.1 M NaCl solution) and Mg-Zn alloy via reducing the kinetics of cathodic reaction (hydrogen evolution reaction (HER)) [44-47]. The OCP of Mg became more negative with addition of Ge as a result of inhibited cathodic reaction. The findings provide a possibility of developing novel corrosion resistant Mg anode materials with satisfying operating potential by alloying with Ge and combination with other elements.

In the present work, we evaluated the possibility of binary Mg-Ge alloy as an anode material for primary aqueous Mg batteries. The influence of Ge addition on Mg-0.1wt% Ca anode has also been investigated from the aspects of corrosion performance and discharge properties. It should be noted that Ge has extremely low solubility in Mg matrix (approximately 0.003 at.% at 602 °C [48]), leading to large fraction of secondary phase when alloying with high Ge content. Thus, only micro-alloyed Mg-Ge and Mg-Ca-Ge alloy were investigated in this work to avoid severe micro-galvanic corrosion induced by coupling of Mg matrix and cathodic secondary phases and to allay the negative effect of CE on anode performance.

2. Experimental procedures

2.1 Materials manufacturing

All the micro-alloyed Mg anodes with nominal composition of Mg-0.1wt% Ca, Mg-0.1wt% Ge and Mg-0.1wt% Ca-0.1wt% Ge were fabricated via conventional gravity casting. Firstly, pure Mg was melted in a boron nitride coated steel crucible placed in a furnace at 760 °C with protection of Ar/SF₆ (5:1) mixed gas. Alloying elements were then added into the Mg melt, holding for 30 min followed by a manual stirring process of 5 min. Afterwards, the melt was poured into a boron nitride coated cylindrical steel mould (60 mm diameter) preheated to 300 °C. The mould filled with melt was then immersed into a water bath for cooling and solidification. The raw materials used were pure Mg ingot, Ca chips and Ge bulks with purity of 99.96 wt%, 99.9 wt% and 99.99 wt% respectively. Pure Mg was recast with the same casting procedure in this work as reference. The actual chemical composition of

all processed materials is shown in Table 1 as analyzed by spark spectrometer (spark OES, Ametek-Spectro) and X-ray micro fluorescence (μ XRF, Bruker). The impurities Fe, Ni and Cu [19, 49-52] that have deleterious influence on Mg corrosion resistance indicate extremely low content below 20 ppm. The content of Si in different materials ranges from 36 to 97 ppm. Note that Si, which has not been widely accepted as a detrimental impurity to Mg, has been demonstrated recently to have significant effect on corrosion resistance of pure Mg even in trace amount in combination with Fe [22, 53]. **Table 1** Chemical composition of recast pure Mg and Mg alloys (wt%).

Materials	Ca	Ge	Fe	Ni	Cu	Al	Mn	Si	Mg
Mg	0.0019	-	0.0015	0.0002	0.0003	0.0095	0.018	0.0086	balance
Mg-0.1Ca	0.07	-	0.0018	0.0011	0.0012	< 0.01	0.017	0.0036	balance
Mg-0.1Ge	-	0.09	0.0019	0.0012	0.0012	< 0.01	0.018	0.0048	balance
Mg-0.1Ca-0.1Ge	0.11	0.11	0.0018	0.0010	0.0010	< 0.01	0.015	0.0060	balance

2.2 Microstructure characterization

All specimens after embedding in resin were carefully ground and polished to obtain high-quality samples for microstructure observation. Grinding process was carried out on silicon carbide papers consecutively up to 4000 grit. Afterwards, samples were polished to remove scratches using a water-free oxide polishing suspension (OPS) containing SiO₂ followed by a cleaning process in ethanol by ultrasonication. After etching with an acetic-picric acid solution, second phase morphology and distribution were observed with a scanning electron microscope (SEM, TESCAN VEGA3) combined with energy dispersive X-ray spectroscopy (EDS) to analyze the element composition. Besides, atomic force microscopy (AFM, Nanowizard, JPK Instruments AG) combined with Scanning Kelvin Probe Force Microscopy (SKPFM) was utilized to measure the Volta potential difference between secondary phase particles and the Mg matrix. The adopted silicon probe supplied by Innovative Solutions Bulgaria Ltd. (Bulgaria) was coated with a Cr/Pt conductive coating and possesses a resonance frequency of 75 kHz and a force constant of 3 N m⁻¹. Electric connection was achieved using a conductive tape between the sample and the grounded AFM stage. The lift height between the probe and sample surface was set as 100 nm. The scanning was conducted on an area of 30 × 30 μ m with a resolution of 512 × 512 pixels immediately after sample polishing via the aforementioned processes.

2.3 Immersion tests

Long-term immersion tests for 7 days were applied to evaluate the corrosion rates of all prepared materials. Note, the electrolyte used for all measurements in this work is unbuffered 3.5 wt% NaCl solution with pH of 5.6 ± 0.2 if other not specified. Hydrogen gas produced by corrosion of immersed samples was collected simultaneously via a widely used set-up combining a funnel and an inverted burette [54]. Plug-in samples of $15 \times 15 \times 5$ mm were hung in the solution with fishing line fastened to a plastic screw inserted into the samples. The weight loss of each sample after testing was determined after removing corrosion products by a diluted chromic acid (200 g L^{-1}). Corrosion rate, P_w (mm y^{-1}), can be calculated based on weight loss via the following formula:

$$P_w = \frac{365 \cdot 24 \cdot 10 \cdot \Delta m}{\rho \cdot A \cdot t} \quad (1)$$

Where Δm is sample weight loss during immersion, g; ρ is density of Mg, g cm^{-3} ; A is sample surface area, cm^2 ; t is immersion time, h. Then, the formula can be simplified as following [23]:

$$P_w = 2.10 W \quad (2)$$

Where W is weight loss rate ($\text{mg cm}^{-1} \text{d}^{-1}$) determined based on immersion tests.

Afterwards, surface morphology of each material after immersion was characterized by the SEM. Immersion test for each material was conducted for three times to ensure data reproducibility. In order to evaluate the corrosion origination and the role of secondary phases in the corrosion behavior of the newly designed Mg-Ca-Ge alloy, a quasi - in situ approach was applied with the same procedures as reported previously by Jin et al.[55]. A specimen was polished and then observed under SEM to record the morphologies of uncorroded secondary phases in specific regions with a relatively low voltage of 10 kV. After that, a short-term immersion (10 min) in 3.5 wt% NaCl solution was carried out, following an extra polishing process for 1 min with OPS to eliminate the possible influence of SEM observation on the corrosion behavior of this alloy. Subsequently, the morphologies of the secondary phases from the previously recorded regions were collected. The specimen was then immersed in chromic acid for 30 s to remove corrosion products. The morphologies of the same regions without corrosion products were also recorded then. For easy access to the regions of interest, some minor tracks were made on the sample surface via an aluminum tweezer in advance.

2.4 Electrochemical measurements

Potentiodynamic polarization curves were obtained using a Gamry interface 1000 potentiostat in 3.5 wt% NaCl solution with a conventional three-electrode cell consisting of a Pt wire counter electrode, a Ag/AgCl reference electrode and a Mg electrode with 1 cm² working surface area. A stabilization period lasted for one hour before each measurement to obtain a relatively stable OCP. Afterwards, anodic polarization curves were collected by scanning from – 5 mV to + 600 mV (vs. OCP) with a scan rate of 1 mV s⁻¹. Besides, cathodic polarization curves following the immersion for 1 and 24 hours were measured separately via scanning from + 5 mV vs. OCP negatively forwards to 400 mV vs. OCP with the same scan rate.

2.5 Discharge testing

Half-cell discharge tests were conducted in the aforementioned three-electrode set-up in 3.5 wt% NaCl solution with all prepared Mg anodes. Two current densities, i.e. 1 and 10 mA cm⁻², were applied. Afterwards, weight loss of each sample due to discharge was determined. Accordingly, utilization efficiency and discharge capacity of each anode were calculated with the following equations [14, 56].

$$\text{Utilization efficiency (\%)} = \frac{W_{theo}}{\Delta W} \times 100\% \quad (3)$$

$$\text{Specific capacity (Ah g}^{-1}\text{)} = \frac{I \times t}{\Delta W} \quad (4)$$

Where I (A) is the discharge current, t (h) is discharge time, ΔW (g) is the actual mass loss of samples during discharge process and W_{theo} (g) is the theoretical mass loss due to faradaic process. ΔW was determined by measuring the mass of samples before discharge and after removal of discharge products. W_{theo} was calculated via the following equation:

$$W_{theo} = \frac{I \times t}{F \times \sum \left(\frac{x_i \times n_i}{m_i} \right)} \quad (5)$$

Where F represents the Faraday constant (26.8 Ah mol⁻¹), x_i , n_i , m_i represent the mass fraction, number of exchanged electrons and atomic weight, respectively, of each element in the materials.

In addition, self-discharge rate during discharge at different current densities was measured via hydrogen evolution tests with the same configuration used in previous work [41]. The measurements were replicated for three times and indicated very good reproducibility. Electrochemical impedance

spectroscopy (EIS) testing was carried out immediately after discharge to evaluate anode activity associated with the surface condition. The scanned frequency range was 100 kHz to 0.1 Hz, and the sinusoidal AC voltage was 10 mV rms. Discharge tests were also performed in a fully assembled custom-made Mg-air cell filled with 3.5 wt% NaCl solution. The cathode material, with a 2.5 cm² working area, was a commercial air cathode based on C/MnO₂ catalyst, while the anode material was the manufactured Mg alloys embedded in resin with an exposed area of approximately 2.3 cm². A commercially cast alloy AZ31, with impurities of 11 ppm Fe, 7 ppm Ni and 19 ppm Cu, was also tested for comparison reason under the same experimental condition. All the anodes were also evaluated in the electrolyte with the aforementioned Mg²⁺ complexing agent additive, i.e. salicylate (SAL). The electrolyte of 0.1 M SAL was prepared by dissolving sodium salicylate (Sigma-Aldrich S3007) in 3.5 wt. % NaCl as background solution. The specific concentration was selected according to the published work of Wang et al.[40]. The initial bulk pH of the solution was adjusted to 7 ± 0.2 by adding NaOH solution, controlled by Metrohm-691 pH meter equipped with a Mettler-Toledo LabExpert Pt-1000-pH glass electrode.

3. Results

3.1 Microstructure

The microstructure of all fabricated materials characterized via SEM is presented in Fig. 1. Further, chemical compositions analyzed by EDS for several randomly selected precipitates from each alloy are shown in Table 2. Obviously, precipitates with different morphologies and distributions are present in all micro-alloyed materials. For the Mg-0.1Ca alloy, the precipitates, appearing as small particles, are CaMgSi as detected by EDS, even though Si content is at a low level in the alloy (36 ppm). Similarly, it has been reported that the existence of trace Si could promote the precipitation of CaMgSi phase in the Mg-Zn-Ca system during solidification [55]. Regarding the binary Mg-0.1Ge alloy, the precipitates are confidently recognized as Mg₂Ge intermetallics as known from the Ge-Mg phase diagram [57] and several published works [46, 58, 59]. The EDS results shown in Table 2 indicate much higher concentration of Mg in the intermetallic due to the tiny size of these precipitates, which leads to the inclusion of Mg matrix in the region assessed by EDS. For the Mg-0.1Ca-0.1Ge alloy, Mg, Ca and Ge

elements are identified in all precipitates by point EDS analysis (Table 2) and elemental mapping (see Fig. 2), indicating the presence of a ternary intermetallic. Besides, it is distinct that the quantity of intermetallics in the Mg-Ca-Ge system is larger than that in binary Mg-Ca and Mg-Ge system, owing to the higher alloying load. Note that there is a lack of ternary phase diagram of Mg-Ca-Ge system and, therefore, the stoichiometry of the intermetallic in this alloy is not well known. Thus, we simply refer to it as $Mg_xCa_yGe_z$. Something noteworthy is that a small quantity of Si (less than 0.5 wt%) is detected in all the precipitates in Mg-0.1Ge and Mg-0.1Ca-0.1Ge alloys. Distinguished from the high quantity of Si in the MgCaSi intermetallic found in Mg-0.1Ca system, the traces of Si in the Mg-0.1Ge and Mg-0.1Ca-0.1Ge alloys is proposed to segregate around the Mg_2Ge and $Mg_xCa_yGe_z$ precipitates (possibly as Mg_2Si or $CaMgSi$) instead of forming new Si-containing intermetallics. As reported by Jung et al. [60], no ternary phase is predicted in Mg-Ge-Si alloy except for a combination of Mg_2Ge - Mg_2Si ($Mg_2Ge_xSi_{1-x}$) without fixed ratio.

[Fig. 1]

[Fig. 2]

Table 2 Chemical compositions of some precipitates marked in Fig. 1 as analyzed by EDS (wt%).

Precipitates	A	B	C	D	E	F	G	H
<i>Mg</i>	91.6	79.6	80.2	94.9	97.0	82.3	87.5	94.8
<i>Ca</i>	4.9	10.5	10.7	/	/	5.4	4.1	1.9
<i>Ge</i>	/	/	/	4.8	2.6	11.8	8.2	3.0
<i>Si</i>	3.5	9.9	9.1	0.3	0.4	0.5	0.2	0.3

3.2 Electrochemical performance

Fig. 3a presents the results of one-hour OCP measurements corresponding to all as-cast materials. All micro-alloyed materials possess remarkably more negative OCP than that of the recast pure Mg. The average OCP values for Mg-0.1Ca, Mg-0.1Ge and Mg-0.1Ca-0.1Ge are -1.83 ± 0.02 , -1.78 ± 0.04 and -1.91 ± 0.01 $V_{Ag/AgCl}$, respectively, comparing to -1.65 ± 0.02 $V_{Ag/AgCl}$ of the recast pure Mg. Apparently, ternary Mg-0.1Ca-0.1Ge shows a more negative OCP than the two binary alloys, demonstrating a good synergy effect of Ca and Ge micro-alloying. The highly negative OCP endows the micro-alloyed alloys with a great possibility to offer high discharge voltage as anode materials. Fig.

3b depicts the anodic polarization curves of all materials after immersion in 3.5 wt% NaCl for one hour. All alloyed Mg exhibits a pitting potential at around $-1.60 \text{ V}_{\text{Ag/AgCl}}$, indicating the formation of a pseudo-protective film on the samples surface. All the curves associated with different alloys are generally overlapped within the potential range more positive than the pitting potential, elucidating similar anodic dissolution kinetics. Slight difference is only found within the potential range from the pitting potential to OCP but is most likely induced by varied OCP values of these alloys resulting from different cathodic HER kinetics as demonstrated in Fig. 3(c, d). Cathodic polarization curves were separately measured after immersion for one hour (Fig. 3c) and 24 hours (Fig. 3d). Regarding one-hour immersion, varied cathodic kinetics corresponding to different materials are demonstrated, specifying that micro-alloying individually with Ca owns the ability of reducing the kinetics of cathodic reaction on pure Mg. Similar effect is found with minor Ge addition, in accordance with the results reported by Deng et al.[37] and Liu et al.[44, 45]. The updated finding here is that micro-alloying with Ca is better than Ge regarding suppressing cathodic HER amid the immersion period of 7 days and the combination of Ca and Ge is demonstrated to be more effective. The suppressed cathodic kinetics drives the cathodic polarization curve to move towards the direction of smaller current densities and, consequently, results in the more negative OCP. After 24-hour immersion, all the micro-alloyed materials maintain suppressed cathodic kinetics comparing to pure Mg. Interestingly, the polarization curves of Mg-0.1Ca and Mg-0.1Ca-0.1Ge partially overlap within the more negative potential range, elucidating that these two materials have similar kinetics of cathodic reaction after this immersion duration. Table 3 lists the current density of cathodic reaction at -2.0 V (vs. Ag/AgCl) derived from these presented cathodic polarization curves measured after one-hour and 24-hour immersion, aiming to evaluate the variation of cathodic kinetics of each material after different immersion time. Obviously, a large increase of the defined current density, by a couple of orders of magnitude, is found regarding the pure Mg, which indicates a remarkable increase of its cathodic kinetics. The concerned current densities of Mg-0.1Ge and Mg-0.1Ca-0.1Ge both remain relatively constant, while a slight decrease is found from Mg-0.1Ca, showing that the cathodic kinetics of Mg-0.1Ca decreases with immersion, presumably related to fast detachment of fine CaMgSi precipitates. Generally, Mg-0.1Ca-0.1Ge possesses the lowest cathodic kinetics after immersion for 1 and 24 hours, being conducive to achieve a low corrosion rate.

[Fig. 3]

Table 3 Current density of cathodic reaction at -2.0 V (vs. Ag/AgCl) derived from cathodic polarization curves shown in Fig. 3c and d. Results of two independent measurements are presented to demonstrate the reproducibility.

Current density $\mu\text{A cm}^{-2}$	After 1 hour		After 24 hours	
	Test #1	Test #2	Test #1	Test #2
Mg	527	620	10180	6690
Mg-0.1Ca	76	99	49	40
Mg-0.1Ge	159	164	120	214
Mg-0.1Ca-0.1Ge	43	39	42	31

3.3 Corrosion properties

Fig 4 illustrates the calculated corrosion rates of all materials based on the weight loss within 7-day immersion. The recast pure Mg exhibits a corrosion rate of nearly 0.6 mm y^{-1} , which is slightly higher than that of high-purity Mg (0.4 mm y^{-1}) reported by Shi et al. [21] and Qiao et al. [20] and intrinsic corrosion rate of ultra-high-purity Mg (0.3 mm y^{-1}) [23]. Likewise, large deviations between each measurement are also found in this work regarding the corrosion determination of pure Mg, resulting from the non-uniform Fe-rich precipitates. Remarkably, the corrosion rate of recast pure Mg is reduced after micro-alloying with 0.1 wt% Ca and Ge whereby corrosion rates of approximately 0.2 mm y^{-1} and 0.3 mm y^{-1} are achieved respectively. Further, combinative minor addition of Ca and Ge results in the lowest corrosion rate, which is similar to that of the binary Mg-0.1Ca and is even slightly below the intrinsic Mg corrosion rate of 0.3 mm y^{-1} [23]. Note that corrosion rates may be even lower if determined with fishing-line specimens instead of plug-in ones as demonstrated by Cao et al. [23]. Fig. 5 shows the surface morphologies of all materials after 7-day immersion tests and removal of corrosion products. Typical filiform-like corrosion is found on pure Mg, while generally uniform corrosion is characteristic for all micro-alloyed Mg. Some discrete corrosion cavities appear on the surface of Mg-0.1Ca alloy, whilst numerous but smaller pits are distinct on Mg-0.1Ge surface. Regarding Mg-0.1Ca-0.1Ge alloy, the corrosion pits after immersion are rather shallow and inconspicuous, at least under the same

magnification. Besides, grinding scratches are still visible from Mg-0.1Ca and Mg-0.1Ca-0.1Ge surface after 7-day immersion, manifesting the grossly high corrosion resistance of these two alloys.

[Fig. 4]

[Fig. 5]

3.4 Electrochemical characteristic of $Mg_xCa_yGe_z$ intermetallic

The electrochemical characteristic of the newfound $Mg_xCa_yGe_z$ intermetallic is first investigated in this work. The Volta potential difference of $Mg_xCa_yGe_z$ intermetallic with respect to Mg matrix is determined via SKPFM, as depicted in Fig. 6. Intriguingly, $Mg_xCa_yGe_z$ shows a negative potential difference to the matrix of ~ -100 mV, probably related to Ca enrichment. The results indicate that $Mg_xCa_yGe_z$ serves as local anode and suffers preferential dissolution during corrosion initiation after immersion, until complete degradation or detachment from alloy surface. To further unveil the anodic essence of the ternary phase with reference to Mg matrix, quasi-in situ corrosion measurements are applied. Relevant results are presented in Fig. 7, demonstrating the surface morphologies of same intermetallic-included regions prior to and after short-term immersion. The results indicate that $Mg_xCa_yGe_z$ intermetallic indeed suffers preferential corrosion prior to adjacent Mg matrix within the initial immersion stage, in accordance with the determined negative Volta potential with respect to the matrix. Besides, images presented in Fig. 7(a-3, b-3) exhibit the corrosion morphology with a striking characteristic, consisting of ambient shallow valleys surrounding deeper cavities in the center. The distinct corrosion morphology is similar to that reported upon a GW93 alloy (Mg-9.2wt%Gd-4.03wt%Y-0.52wt%Zr) [61], which contains Mg-Gd-Y anodic second phases. The central deeper cavities are proposed to be the result of preferential dissolution of anodic phases. Afterwards, corrosion propagates around the previous corrosion cavities and leads to the surrounding shallow corrosion areas. The difference between our work and the mentioned one is that corrosion is remarkably low for Mg-0.1Ca-0.1Ge alloy. Therefore, after long time immersion, severe pitting corrosion that is found regarding the reported GW93 alloy does not occur on the micro-alloyed Mg-Ca-Ge system in this work.

[Fig. 6]

[Fig. 7]

3.5 Discharge testing in half-cell

The discharge properties of all micro-alloyed Mg anodes are primarily evaluated **via half-cell testing**. **Fig. 8** illustrates the potential variation with time for all anodes during discharge at 1 and 10 mA cm⁻². Obviously, minor addition of Ca and Ge both **result** in more negative discharge potential than the pure Mg at two studied current densities. Mg-0.1Ge anode shows similar potential to Mg-0.1Ca, and the addition of Ge to Mg-0.1Ca merely induces a slight improvement to the discharge potential. The slightly decreased potential at 1 mA cm⁻² with time is possibly due to increased surface area. The potential difference among the three micro-alloyed anodes is around 10 mV, while comparing to pure Mg the difference is approximately 40 – 60 mV. **Fig. 9** presents the utilization efficiency and discharge capacity of all studied anodes calculated after discharge at 1 and 10 mA cm⁻². Not surprisingly, micro-alloyed Mg-0.1Ca shows considerably enhanced utilization efficiency than the recast pure Mg as well as **higher** discharge capacity at both current densities, agreeing well with the results in our previous work [37]. The main finding here is that micro-alloyed Mg-0.1Ge and Mg-0.1Ca-0.1Ge also have much higher efficiency and capacity than pure Mg anode, although no improvement is found when compared with Mg-0.1Ca anode. All the micro-alloyed anodes show utilization efficiency of nearly 50% at 1 mA cm⁻² and 58% at 10 mA cm⁻², **higher than that of most previously proposed Mg anodes, particularly under low current densities as summarized in Table 4**. **Fig. 10** illustrates the surface morphologies of all micro-alloyed anodes after discharge and removal of discharge products. A few localized cavities are visible, either macroscopically or microscopically, from the surface after discharge at 1 mA cm⁻² for 15 h presented in **Fig. 10(a-d)**, being the manifestation of detachment of chunks. **Chunk effect is also apparently demonstrated by the cross-sectional morphology after discharge at 1 mA cm⁻² presented in Fig. 10(i, j)**. **Exfoliation of these chunks during discharge decreases the anode efficiency to some extent**. In the case of 10 mA cm⁻², the surfaces of all micro-alloyed anodes after discharge are generally uniform with absence of visible deep cavities (**Fig. 10(e-h)**), **elucidating more homogeneous anodic dissolution in comparison to that at low current density**.

[Fig. 8]

[Fig. 9]

[Fig. 10]**Table 4** Utilization efficiency (UE) of diverse Mg anodes in 3.5 wt% NaCl solution under low current densities.

Mg anode	Alloying load	Condition	UE	Current density	Reference
Mg-0.1Ca	0.1 wt%	as-cast	49%	1 mA cm ⁻²	this work
Mg-0.1Ge	0.1 wt%		50%		
Mg-0.1Ca-0.1Ge	0.2 wt%		48%		
AZ91	10.1 wt%	extruded	25%	2.5 mA cm ⁻²	[62]
AZ91-Ca	11.5 wt%		32%		
AZ91-La	10.4 wt%		24%		
AZ91-Sm	10.5 wt%		18%		
AZ91-Ca-Sm-La	12.2 wt%		25%		
Mg-Zn-Y	7.1 wt%	as-cast	39%	2.5 mA cm ⁻²	[63]
	11 wt%		36%		
Mg-Zn-Zr	6.7 wt%		33%		
AZ80	9.1 wt%	as-cast	22%	1.5 mA cm ⁻²	[64]
		ultrasonic treated	32%		
		electromagnetic field treated	23%		
AZ61	7.1 wt%	as-cast	41%	2.5 mA cm ⁻²	[65]
		rolled	45%		
AZ61-LA	7.6 wt%	as-cast	44%		
		rolled	47%		
Mg	99.8 wt% Mg	plate	38%	1 mA cm ⁻²	[66]
EV31A	5.1 wt%		42%		
ZE10A	2 wt%		34%		
Mg-Al	9 wt%	as-cast and then	30%	2.5 mA cm ⁻²	[67]
Mg-Al-In	10 wt%	annealed	32%		
AZ91	10 wt%		30%		
Mg-Al	3 wt%	as-cast and then	38%	2.5 mA cm ⁻²	[68]
Mg-Al-Sn	4 wt%	annealed	52%		
Mg-Al-Ga	4 wt%		53%		
Mg-Al-In	4 wt%		42%		
AZ31	4 wt%		40%		

3.6 Mg-air battery tests

To evaluate the discharge properties of prepared Mg-0.1Ca, Mg-0.1Ge and Mg-0.1Ca-0.1Ge alloy as anode materials for primary Mg batteries, discharge testes are also performed in a custom-made Mg-air full cell. A commercially cast AZ31 alloy, which has been widely accepted as anode material for

aqueous Mg batteries, is included for comparison. Fig. 11 presents the cell voltage profile of the Mg-air cell adopted with different anodes. Note that the adopted AZ31 anode in this work provides voltage of 1.16 V at 10 mA cm^{-1} , comparable to the existing value (1.2 V) for AZ31 from the work of Ma et al.[69]. Mg-0.1Ge and Mg-0.1Ca-0.1Ge both provide the Mg-air cell with significantly improved cell voltage comparing to the AZ31 anode, e.g. 1.26 V at 10 mA cm^{-1} . Besides, the utilization efficiency of AZ31 anode, around 36% at 1 mA cm^{-2} as reported in our previous work [41], is also inferior in comparison with M-0.1Ge and Mg-0.1Ca-0.1Ge, 50% as mentioned above. In addition, the two micro-alloyed alloys also exhibit similar discharge properties to the Mg-0.1Ca anode, which is a newly developed high quality anode material [37]. Thus, as good candidates, they provide additional options for anode materials concerning developing high performance primary Mg system. Interestingly, the minor addition of Ge to Mg-0.1Ca anode do not induce large enhancement regarding discharge potential or voltage measured in half-cell or Mg-air full cell.

[Fig. 11]

4. Discussion

4.1 Effect of Ca/Ge micro-alloying on corrosion performance

The present study indicates that low corrosion rates are achieved by Ca/Ge micro-alloying. The reduced corrosion rates are attributed to the inhibited cathodic kinetics and a pseudo-protective surface film. The lower cathodic reaction rates of Mg-0.1Ca and Mg-0.1Ca-0.1Ge result in slower corrosion rates than that of Mg-0.1Ge. Cathodic reaction kinetics of Mg-0.1Ca-0.1Ge is weaker than that of Mg-0.1Ca merely at the initial immersion stage and then tends to be similar, thus leading to the alike corrosion rate. Contemporarily, restricting kinetics of HER has been considered as a more logical approach for developing highly corrosion resistant Mg alloys with the inspiration of alloying element As [70, 71] and other Group 14 and Group 15 elements, like Ge [44-46]. The mechanism for kinetics restriction by these alloying elements remains unclear, but is most possibly related to restriction of impurity action and re-deposition. Cathodic poisons, such as As, is supposed to deposit and cover the surface of impurities-rich particles, which serve as primarily cathodic sites for HER, thus reducing the HER rate. Besides, the composition of surface oxide/hydroxide film is possibly altered by these

elements and then leads to the suppressed cathodic kinetics, notwithstanding the possible influence has not been amply investigated. The results presented in this work (Fig. 3c and d) show that in the case of the recast pure Mg the HER increases with immersion time. This increment upon pure Mg is presumably related to impurity enrichment and build-up of a hydroxide film on Mg surface. The enrichment of noble impurities, like Fe at Mg surface as a result of re-deposition process [50], increases the cathodic HER kinetics to a certain extent, although some works have demonstrated the Fe enrichment efficiency is low [72, 73]. Besides, as reported, an ultra-high-purity Mg (0.1 ppm Fe) showed accelerated cathodic HER kinetics after anodic polarization comparing to the non-polarized state, elucidating possible influence of hydroxide film on cathodic reaction [52]. By contrast, there is no such an increase in other systems with Ca and Ge. It seems the effect of noble impurities and hydroxide film on HER is restricted by the alloying elements, speculatively attributed to altered film composition and reduced impurities enrichment. Additionally, kinetics restriction is also accessible through alloying elements with capability of sequestering impurities via either reducing the impurities contents during solidification or alleviating the cathodic activity of impurity-rich particles by altering the particles chemistry. Regrettably, few elements with this function are found, with Mn [49, 74] and Y [75] as representatives. Herein, it is not fully clear which factors contribute to the restricted cathodic kinetics of Mg-0.1Ca, Mg-0.1Ge and Mg-0.1Ca-0.1Ge alloys. Nevertheless, it is apparent that addition of 0.1% Ca as well as the combination of minor Ca and Ge is more effective than Ge regarding kinetic control, as shown in Fig. 3.

The effect of induced intermetallics in fabricated lean alloys should also be considered, as the intermetallic normally possesses different electrochemical potential with respect to Mg matrix, being drivers for severe galvanic corrosion. Mg₂Ge phase exhibits a positive potential difference of ~ 400 mV with respect to the matrix of Mg-0.3 wt% Ge alloy as reported by Liu et al.[44], whilst merely ~50 mV in Mg-0.5Zn-0.2Ge system reported by Jiang et al.[46] Nevertheless, only superficial corrosion occurs around this cathodic phase as indicated by the mentioned work and Fig. 5 in this study. Therefore, it is reasonable to conclude that the low corrosion rate of micro-alloyed Mg-Ge alloy is attributed at least partially to the absence of severe galvanic corrosion related to Mg₂Ge phase. Alike, CaMgSi intermetallic in Mg-0.1Ca alloy also possesses higher electrochemical potential than the matrix, ~ 400

mV as determined by Ben-Hamu et al.[76] and ~200 mV by Mohedano et al.[77]. However, this kind of cathodic intermetallic also does not induce severe localized corrosion as proved by the surface morphology in Fig. 5. Only some shallow corrosion cavities are seen even after immersion for 7 days in the highly corrosive 3.5 wt% NaCl solution, possibly due to small size and low quantity of CaMgSi particles. Regarding Mg-0.1Ca-0.1Ge alloy, $Mg_xCa_yGe_z$ ternary phase acts as micro-anode with respect to Mg matrix, leading to its preferential dissolution and protection to matrix. Subsequently, this anodic phase is completely degraded or loss contact with the solution due to accumulation of corrosion products. In this case, corrosion starts upon the matrix, particularly around the dissolved secondary phases. Due to inhibited cathodic HER kinetics and absence of severe galvanic corrosion in this stage, the Mg-0.1Ca-0.1Ge matrix merely suffers superficial corrosion as shown in Fig. 5. Summarizing, the inhibited cathodic kinetics of HER and low amount of secondary phase particles contribute to the low corrosion rates of these alloys micro-alloyed with Ca/Ge, which are comparable to intrinsic Mg corrosion rate.

4.2 Effect of Ca/Ge micro-alloying on discharge properties

It is noteworthy that the difference of discharge potential for all studied anodes is much smaller comparing to the difference of OCP measured either before (up to 260 mV, Fig. 3a) or after discharge (up to 280 mV, Fig. 12a). In principle, apart from OCP, the discharge potential of Mg anodes is tightly dependent on the over potential under applied anodic current, which is determined by anodic dissolution kinetics and surface film conditions. EIS measured immediately after discharge is performed to evaluate the electrode activity of all anodes as presented in Fig. 12b. The lowest scan frequency was set as 0.1 Hz, due to the non-stationarity of the active surface caused by discharge. Consequently, regarding all the alloys only one capacitive loop is distinct within the whole frequency range. By contrast, for the recast pure Mg, some scattered data points appear in the low frequency range. Although the interpretation for EIS of Mg is still controversial, the impedance of each anode can be roughly estimated and compared with each other to provide information concerning different electrode activity. Apparently, the recast pure Mg exhibits the highest activity, as forecasted by the lowest impedance value, indicating its fastest activity during discharge, which contributes to the mild difference between the discharge potential of Mg and other alloys. Mg-0.1Ge and Mg-0.1Ca are much alike in OCP as well

as overall impedance value after discharge (at 10 mA cm⁻² for 0.5 hour), implying similar activity and being the reason for the similar discharge potential. In comparison, Mg-0.1Ca-0.1Ge anode still maintains more negative OCP even after discharge, approximately $-1.90 V_{Ag/AgCl}$, comparing to $-1.75 V_{Ag/AgCl}$ for binary Mg-0.1Ca and Mg-0.1Ge. However, this ternary alloy anode shows a remarkably higher impedance value measured after discharge, indicating more sluggish electrode activity in comparison to that of the two binary alloy anodes. Thus, its discharge potential has not been further improved even in the case of significantly negative OCP. The sluggish activity of Mg-0.1Ca-0.1Ge anode is possibly partially related to a more protective surface film of discharge products. In this case, electrolyte additives, like the aforementioned Mg²⁺ complexing agents, is favorable for achieving better discharge potential, with the benefit of highly negative OCP of micro-alloyed Mg-Ca-Ge anodes.

[Fig. 12]

As mentioned in the Introduction section, utilization efficiency and capacity of Mg anodes are associated with chunk effect (CE) and real-time self-discharge rate with applied anodic current, rather than corrosion rate at OCP [41]. Hence, the self-discharge rate of all prepared anodes was determined by real-time hydrogen evolution and is presented in Fig. 13. Notably, all the micro-alloyed anodes exhibit suppressed real-time hydrogen evolution rate, implying lower self-discharge rate, comparing to recast pure Mg anode during discharge at different current densities. However, no obvious difference is seen regarding the hydrogen evolution of the three micro-alloyed anodes, even though they show different corrosion rates measured at OCP condition as shown in Fig. 4. Interestingly, all the three alloy anodes show stable hydrogen evolution behavior after a short stabilization at initial stage. The rate of hydrogen generation is approximately 0.3 ml cm⁻² h⁻¹ at 1 mA cm⁻² and 3.0 ml cm⁻² h⁻¹ at 10 mA cm⁻². Accordingly, the self-discharge current densities calculated via Faraday's law are 0.67 and 6.66 mA cm⁻² at 1 and 10 mA cm⁻², respectively. Thereafter, the utilization efficiency without consideration of efficiency loss by CE (η) can be estimated roughly via the following formula:

$$\eta = \frac{i_{applied}}{i_{applied} + i_{self-discharge}} \quad (6)$$

where $i_{applied}$ is the applied current density, and $i_{self-discharge}$ is the calculated self-discharge current density associated with hydrogen evolution. The estimated η is 60.0% when discharge at both 1 and 10

mA cm⁻², respectively. It is noticeable that the actual utilization efficiency at 10 mA cm⁻², around 58%, is similar to the estimated value (60.0%), indicating negligible efficiency loss caused by CE, **which is attributed to the uniform anodic dissolution as shown in Fig. 10 (e-h)**. By contrast, the actual utilization efficiency at 1 mA cm⁻², nearly 50%, is lower than the estimated value (59.9%), implying an apparent efficiency loss of approximately 10% by CE **(related to the localized cavities shown in Fig. 10 (b-d))**. Nevertheless, this 10% efficiency loss by CE is much lower comparing to that of high purity Mg and some commercially alloy anodes, 20% - 45% at the same current density as reported in our previous work [41]. **To conclude**, micro-alloying of Ca and Ge enables Mg anodes to achieve higher utilization efficiency (50% and 60% at 1 and 10 mA cm⁻² respectively) via reduced self-discharge rate and suppressed occurrence of chunk effect.

[Fig. 13]

4.3 Anode performance in additive-containing electrolyte

As mentioned above, the highly negative OCP of Mg-0.1Ca-0.1Ge alloy provides a possibility to achieve further enhanced battery voltage with adoption of electrolyte additives, like Mg²⁺ complexing agents. To prove this hypothesis, cell voltage of the custom-made Mg-air battery adopting varied anode materials **was** measured in 3.5 wt% NaCl with 0.1 M salicylate (SAL) and is shown in Fig. 14. The voltage profile measured in blank 3.5 wt% NaCl extracted from Fig. 11 is included for the sake of comparison. Predictably, the battery with the same anode material exhibits higher cell voltage when 0.1 M SAL is added into the electrolyte, since SAL is Mg²⁺ complexing agent with the capability of hindering the formation of Mg(OH)₂ film. The boosted voltage is attributed **to the decreased voltage drop associated with absence of thick hydroxide film**. Something noteworthy is that the battery with Mg-0.1Ca-0.1Ge anode shows remarkably improved voltage than that based on Mg-0.1Ca anode **in SAL-containing electrolyte**, in spite of the similar voltage in the electrolyte without SAL. The difference might be due to the varied protection ability of surface film formed in blank 3.5 wt% NaCl as indicated by EIS presented in Fig. 12b. Regarding Mg-0.1Ca-0.1Ge, more overvoltage related to surface film is released after adding SAL via impeding the formation of Mg(OH)₂, leading to the higher operating voltage. The results indicate that the micro-alloyed Mg-0.1Ca-0.1Ge alloy is capable of providing better

battery properties than Mg-0.1Ca, particularly in additive-containing electrolytes. In such a case, more work is desirable for optimizing the electrolyte additives and elucidating their effect on the novel Mg-Ca-Ge anode.

[Fig. 14]

5. Conclusions

Herein, the corrosion and discharge properties of micro-alloyed Mg-0.1%Ge (hereafter weight percent) as an anode material for primary Mg battery are evaluated in comparison to newly developed high performance Mg-0.1%Ca anode. Besides, the synergetic effect of micro-alloying of Ge and Ca to Mg anode is investigated in terms of microstructure, corrosion behavior and discharge properties. The following conclusion can be drawn:

1) Restriction of cathodic HER kinetics via minor Ge alloying is inferior compared to that of Ca, leading to the faster corrosion rate of Mg-0.1%Ge alloy than Mg-0.1%Ca. Nevertheless, the self-discharge rate of Mg-0.1%Ge anode is similar to that of Mg-0.1%Ca, contributing to their alike high utilization efficiency ($\sim 60\%$ at 10 mA cm^{-2}) and superior discharge capacity.

2) The addition of 0.1% Ge decreases the cathodic kinetics of Mg-0.1%Ca alloy, albeit only at initial immersion stage, implying a positive synergetic effect of Ge and Ca on cathodic HER kinetics restriction. Consequently, Mg-0.1%Ca-0.1%Ge alloy exhibits a low corrosion rate (0.2 mm y^{-1} in 3.5 wt% NaCl solution) within 7-day exposure in the solution.

3) Mg-0.1%Ca-0.1%Ge possesses highly negative OCP owing to the intensively restricted cathodic reaction, showing a great promise to offer higher voltage for Mg batteries. However, it exhibits similar voltage to micro-alloyed Mg-Ca and Mg-Ge anodes in 3.5% NaCl electrolyte, due to large voltage drop caused by a more protective film on the surface.

4) In electrolyte containing 0.1 M salicylate, Mg-0.1%Ca-0.1%Ge anode provides higher voltage (1.70 V at 1 mA cm^{-2}) in comparison to Mg-0.1%Ca anode (1.63 V) due to the absence of thick Mg(OH)_2 film.

5) Both Mg-0.1%Ge and Mg-0.1%Ca-0.1%Ge anodes show good discharge properties, which are better than those of AZ31 and comparable to Mg-0.1%Ca anode. Therefore, they are also good

candidates for anode materials of primary batteries and, meanwhile, provide more options for the development of high performance Mg batteries considering the necessity of optimizing anode geometry and electrolyte composition.

Acknowledgement

Bahram Vaghefinazari is sincerely acknowledged for the discussion on experimental results. M. Deng, L. Wang and P. Jiang are grateful for the support from China Scholarship Council concerning the award of fellowship No. 201606370031, No. 201706370183 and No. 201606310043. D. Snihirova acknowledges SeaMag project for financial support (MarTera ERA-NET cofund).

Data availability

The raw/processed data required to reproduce these findings cannot be shared at this time as the data also forms part of an ongoing study.

Reference

- [1] David Linden, T.B. Reddy, Handbook of Batteries, McGraw-Hill, New York, 2002.
- [2] C Daniel, J. Besenhard, Handbook of Battery Materials, Wiley-VCH, Weinheim, 2012.
- [3] F. Cheng, J. Chen, Metal-air batteries: from oxygen reduction electrochemistry to cathode catalysts, Chem. Soc. Rev. , 41 (2012) 2172-2192. <https://doi.org/10.1039/c1cs15228a>.
- [4] T. Zhang, Z. Tao, J. Chen, Magnesium–air batteries: from principle to application, Mater. Horiz., 1 (2014) 196-206. <https://doi.org/10.1039/c3mh00059a>.
- [5] Md. Rahman, X. Wang, C. Wen, High Energy Density Metal-Air Batteries: A Review, J. Electrochem. Soc. , 160 (2013) A1759-A1771. <https://doi.org/10.1149/2.062310jes>.
- [6] M. Deng, D. Höche, D. Snihirova, L.Q. Wang, B. Vaghefinazari, S.V. Lamaka, M.L. Zheludkevich, Aqueous Mg batteries, in: M. Fichtner (Ed.) Magnesium Batteries: Research and Applications, Royal Society of Chemistry, United Kingdom, 2019, pp. 275-308. <https://doi.org/10.1039/9781788016407-00275>.
- [7] N.G. Wang, R.C. WANG, C.Q. Peng, C.W. Hu, Y. Feng, B. Peng, Research progress of magnesium anodes and their applications in chemical power sources, Transactions of Nonferrous

- Metals Society of China, 24 (2014) 2427-2439. [https://doi.org/10.1016/S1003-6326\(14\)63367-7](https://doi.org/10.1016/S1003-6326(14)63367-7).
- [8] R. Mohtadi, F. Mizuno, Magnesium batteries: Current state of the art, issues and future perspectives, *Beilstein J Nanotechnol*, 5 (2014) 1291-1311. <https://doi.org/10.3762/bjnano.5.143>.
- [9] R. Udhayan, N. Muniyandi, P.B. mathur, Studies on magnesium and its alloys in battery electrolytes, *British Corroison Journal*, 27 (1992) 68-71.
<https://doi.org/10.1179/000705992798268927>.
- [10] D. Höche, S.V. Lamaka, B. Vaghefinazari, T. Braun, R.P. Petrauskas, M. Fichtner, M.L. Zheludkevich, Performance boost for primary magnesium cells using iron complexing agents as electrolyte additives, *Sci Rep*, 8 (2018) 7578. <https://doi.org/10.1038/s41598-018-25789-8>.
- [11] Y. Li, J. Ma, G. Wang, F. Ren, Y. Zhu, Y. Song, Investigation of Sodium Phosphate and Sodium Dodecylbenzenesulfonate as Electrolyte Additives for AZ91 Magnesium-Air Battery, *J. Electrochem. Soc.*, 165 (2018) A1713-A1717. <https://doi.org/10.1149/2.0581809jes>.
- [12] M. Shinohara, E. Araki, M. Mochizuki, T. Kanazawa, K. Suyehiro, Practical application of a sea-water battery in deep-sea basin and its performance, *J. Power Sources* 187 (2009) 253-260.
<https://doi.org/10.1016/j.jpowsour.2008.10.105>.
- [13] B.V. Ratnakumar, Passive films on magnesium anodes in primary batteries, *J. Appl. Electrochem.*, 18 (1988) 268-279. <https://doi.org/10.1007/BF01009274>.
- [14] M. Yuasa, X. Huang, K. Suzuki, M. Mabuchi, Y. Chino, Discharge properties of Mg–Al–Mn–Ca and Mg–Al–Mn alloys as anode materials for primary magnesium–air batteries, *J. Power Sources* 297 (2015) 449-456. <https://doi.org/10.1016/j.jpowsour.2015.08.042>.
- [15] T. Zheng, Y. Hu, Y. Zhang, S. Yang, F. Pan, Composition optimization and electrochemical properties of Mg-Al-Sn-Mn alloy anode for Mg-air batteries, *Materials & Design*, 137 (2018) 245-255. <https://doi.org/10.1016/j.matdes.2017.10.031>.
- [16] L.Q. Wang, R.C. Wang, Y. Feng, M. Deng, N.G. Wang, Effect of Al and Pb Contents on the Corrosion Electrochemical Properties and Activation of Mg-Al-Pb Alloy Anode, *J. Electrochem. Soc.*, 164 (2017) A438-A446. <https://doi.org/10.1149/2.1211702jes>.
- [17] K. Gusieva, C.H.J. Davies, J.R. Scully, N. Birbilis, Corrosion of magnesium alloys: the role of alloying, *Int. Mater. Rev.*, 60 (2014) 169-194. <https://doi.org/10.1179/1743280414y.0000000046>.

- [18] Y.D. Milusheva, R.I. Boukoureshlieva, S.M. Hristov, A.R. Kaisheva, Environmentally-clean Mg-air electrochemical power sources, *Bulgarian Chemical Communications*, 43 (2011) 42-47.
- [19] S.V. Lamaka, B. Vaghefinazari, D. Mei, R.P. Petrauskas, D. Höche, M.L. Zheludkevich, Comprehensive screening of Mg corrosion inhibitors, *Corros. Sci.*, 128 (2017) 224-240.
<https://doi.org/10.1016/j.corsci.2017.07.011>.
- [20] Z. Qiao, Z. Shi, N. Hort, N.I. Zainal Abidin, A. Atrens, Corrosion behaviour of a nominally high purity Mg ingot produced by permanent mould direct chill casting, *Corros. Sci.*, 61 (2012) 185-207.
<https://doi.org/10.1016/j.corsci.2012.04.030>.
- [21] Z. Shi, A. Atrens, An innovative specimen configuration for the study of Mg corrosion, *Corros. Sci.*, 53 (2011) 226-246. <https://doi.org/10.1016/j.corsci.2010.09.016>.
- [22] L. Yang, X. Zhou, S.-M. Liang, R. Schmid-Fetzer, Z. Fan, G. Scamans, J. Robson, G. Thompson, Effect of traces of silicon on the formation of Fe-rich particles in pure magnesium and the corrosion susceptibility of magnesium, *J. Alloys Compd.*, 619 (2015) 396-400.
<https://doi.org/10.1016/j.jallcom.2014.09.040>.
- [23] F. Cao, Z. Shi, J. Hofstetter, P.J. Uggowitzer, G. Song, M. Liu, A. Atrens, Corrosion of ultra-high-purity Mg in 3.5% NaCl solution saturated with Mg(OH)₂, *Corros. Sci.*, 75 (2013) 78-99.
<https://doi.org/10.1016/j.corsci.2013.05.018>.
- [24] G. Xin, X. Wang, C. Wang, J. Zheng, X. Li, Porous Mg thin films for Mg-air batteries, *Dalton Trans.*, 42 (2013) 16693-16696. <https://doi.org/10.1039/c3dt52482e>.
- [25] C. Li, F. Cheng, W. Ji, Z. Tao, J. Chen, Magnesium microspheres and nanospheres: Morphology-controlled synthesis and application in Mg/MnO₂ batteries, *Nano Research*, 2 (2009) 713-721.
<https://doi.org/10.1007/s12274-009-9075-y>.
- [26] W. Li, C. Li, C. Zhou, H. Ma, J. Chen, Metallic Magnesium Nano/Mesoscale Structures: Their Shape-Controlled Preparation and Mg/Air Battery Applications, *Angewandte Chemie*, 118 (2006) 6155-6158. <https://doi.org/10.1002/ange.200600099>.
- [27] J. Liu, H. Wang, Q. Yuan, X. Song, A novel material of nanoporous magnesium for hydrogen generation with salt water, *J. Power Sources* 395 (2018) 8-15.
<https://doi.org/10.1016/j.jpowsour.2018.05.062>.

- [28] I.V. Okulov, S.V. Lamaka, T. Wada, K. Yubuta, M.L. Zheludkevich, J. Weissmüller, J. Markmann, H. Kato, Nanoporous magnesium, *Nano Research*, 11 (2018) 6428-6435.
<https://doi.org/10.1007/s12274-018-2167-9>.
- [29] A. Pardo, M.C. Merino, A.E. Coy, F. Viejo, R. Arrabal, S. Feliú, Influence of microstructure and composition on the corrosion behaviour of Mg/Al alloys in chloride media, *Electrochim. Acta* 53 (2008) 7890-7902. <https://doi.org/10.1016/j.electacta.2008.06.001>.
- [30] N. Wang, Y. Mu, W. Xiong, J. Zhang, Q. Li, Z. Shi, Effect of crystallographic orientation on the discharge and corrosion behaviour of AP65 magnesium alloy anodes, *Corrosion Science*, 144 (2018) 107-126. <https://doi.org/10.1016/j.corsci.2018.08.003>.
- [31] X. Liu, S. Liu, J. Xue, Discharge performance of the magnesium anodes with different phase constitutions for Mg-air batteries, *J. Power Sources* 396 (2018) 667-674.
<https://doi.org/10.1016/j.jpowsour.2018.06.085>.
- [32] Y. Shi, C. Peng, Y. Feng, R. Wang, N. Wang, Microstructure and electrochemical corrosion behavior of extruded Mg–Al–Pb–La alloy as anode for seawater-activated battery, *Materials & Design*, 124 (2017) 24-33. <https://doi.org/10.1016/j.matdes.2017.03.058>.
- [33] J. Li, B. Zhang, Q. Wei, N. Wang, B. Hou, Electrochemical behavior of Mg-Al-Zn-In alloy as anode materials in 3.5 wt.% NaCl solution, *Electrochim. Acta* 238 (2017) 156-167.
<https://doi.org/10.1016/j.electacta.2017.03.119>.
- [34] K.A. Unocic, H.H. Elsentriecy, M.P. Brady, H.M.M. III, G.L. Song, M. Fayek, R.A. Meisner, B. Davis, Transmission Electron Microscopy Study of Aqueous Film Formation and Evolution on Magnesium Alloys, *J. Electrochem. Soc.* , 161 (2014) C302-C311.
<https://doi.org/10.1149/2.024406jes>.
- [35] J.H. Nordlien, K. Nisancioglu, Morphology and Structure of Oxide Films Formed on MgAl Alloys by Exposure to Air and Water, *J. Electrochem. Soc.* , 143 (1996) 2564-2572.
<https://doi.org/10.1149/1.1837048>.
- [36] N. Wang, R. Wang, C. Peng, Y. Feng, X. Zhang, Influence of aluminium and lead on activation of magnesium as anode, *Transactions of Nonferrous Metals Society of China*, 20 (2010) 1403-1411.
[https://doi.org/10.1016/s1003-6326\(09\)60312-5](https://doi.org/10.1016/s1003-6326(09)60312-5).

- [37] M. Deng, D. Höche, S.V. Lamaka, D. Snihirova, M.L. Zheludkevich, Mg-Ca binary alloys as anodes for primary Mg-air batteries, *J. Power Sources* 396 (2018) 109-118.
<https://doi.org/10.1016/j.jpowsour.2018.05.090>.
- [38] M. Deng, D. Höche, S.V. Lamaka, L. Wang, M.L. Zheludkevich, Revealing the impact of second phase morphology on discharge properties of binary Mg-Ca anodes for primary Mg-air batteries, *Corros. Sci.* , 153 (2019) 225-235. <https://doi.org/10.1016/j.corsci.2019.03.050>.
- [39] B. Vaghefinazari, D. Höche, S.V. Lamaka, D. Snihirova, M.L. Zheludkevich, Tailoring the Mg-air primary battery performance using strong complexing agents as electrolyte additives, *J. Power Sources* 453 (2020). <https://doi.org/10.1016/j.jpowsour.2020.227880>.
- [40] L. Wang, D. Snihirova, M. Deng, B. Vaghefinazari, S.V. Lamaka, D. Höche, M.L. Zheludkevich, Tailoring electrolyte additives for controlled Mg-Ca anode activity in aqueous Mg-air batteries, *J. Power Sources* 460 (2020) 228106. <https://doi.org/10.1016/j.jpowsour.2020.228106>.
- [41] M. Deng, L. Wang, D. Höche, S.V. Lamaka, D. Snihirova, B. Vaghefinazari, M.L. Zheludkevich, Clarifying the decisive factors for utilization efficiency of Mg anodes for primary aqueous batteries, *J. Power Sources* 441 (2019) 227201. <https://doi.org/10.1016/j.jpowsour.2019.227201>.
- [42] G.A. Marsh, E. Schaschl, The Difference Effect and the Chunk Effect, *J. Electrochem. Soc.* , 107 (1960) 960-965. <https://doi.org/10.1149/1.2427579>
- [43] M.E. Straumanis, B.K. Bhatia, Disintegration of Magnesium While Dissolving Anodically in Neutral and Acidic solutions, *J. Electrochem. Soc.* , 110 (1963) 357-360.
<https://doi.org/10.1149/1.2425763>.
- [44] R.L. Liu, M.F. Hurley, A. Kvryan, G. Williams, J.R. Scully, N. Birbilis, Controlling the corrosion and cathodic activation of magnesium via microalloying additions of Ge, *Sci Rep*, 6 (2016) 28747. <https://doi.org/10.1038/srep28747>.
- [45] R.L. Liu, J.R. Scully, G. Williams, N. Birbilis, Reducing the corrosion rate of magnesium via microalloying additions of group 14 and 15 elements, *Electrochim. Acta* 260 (2018) 184-195.
<https://doi.org/10.1016/j.electacta.2017.11.062>.
- [46] P. Jiang, C. Blawert, R. Hou, N. Scharnagl, J. Bohlen, M.L. Zheludkevich, Microstructural influence on corrosion behavior of MgZnGe alloy in NaCl solution, *J. Alloys Compd.* , 783 (2019)

179-192. <https://doi.org/10.1016/j.jallcom.2018.12.296>.

[47] R.L. Liu, Z.R. Zeng, J.R. Scully, G. Williams, B. Birbilis, Simultaneously improving the corrosion resistance and strength of magnesium via low levels of Zn and Ge additions, *Corros. Sci.* , 140 (2018) 18-29. <https://doi.org/10.1016/j.corsci.2018.06.027>.

[48] A.A. Nayeb-Hashemi, J.B. Clark, R.W. Olesinski, G.J. Abbaschian, The Ge-Mg (Germanium-Magnesium) System.pdf, *Bulletin of Alloy Phase Diagrams*, 5 (1984) 359-365.
<https://doi.org/10.1007/BF02872950>.

[49] G.L. Song, A. Atrens, Corrosion Mechanisms of magnesium, *Advanced Engineering Materials*, 1 (1999) 11-33. [https://doi.org/10.1002/\(SICI\)1527-2648\(199909\)1:1<11::AID-ADEM11>3.0.CO;2-N](https://doi.org/10.1002/(SICI)1527-2648(199909)1:1<11::AID-ADEM11>3.0.CO;2-N).

[50] D. Höche, C. Blawert, S.V. Lamaka, N. Scharnagl, C. Mendis, M.L. Zheludkevich, The effect of iron re-deposition on the corrosion of impurity-containing magnesium, *Phys. Chem. Chem. Phys.* , 18 (2016) 1279-1291. <https://doi.org/10.1039/c5cp05577f>.

[51] S.V. Lamaka, D. Höche, R.P. Petrauskas, C. Blawert, M.L. Zheludkevich, A new concept for corrosion inhibition of magnesium: Suppression of iron re-deposition, *Electrochem. Commun.* , 62 (2016) 5-8. <https://doi.org/10.1016/j.elecom.2015.10.023>.

[52] S. Fajardo, G.S. Frankel, Effect of impurities on the enhanced catalytic activity for hydrogen evolution in high purity magnesium, *Electrochim. Acta* 165 (2015) 255-267.
<https://doi.org/10.1016/j.electacta.2015.03.021>.

[53] L. Yang, X. Zhou, M. Curioni, S. Pawar, H. Liu, Z. Fan, G. Scamans, G. Thompson, Corrosion Behavior of Pure Magnesium with Low Iron Content in 3.5 wt% NaCl solution, *J. Electrochem. Soc.* , 162 (2015) C362-C368. <https://doi.org/10.1149/2.1041507jes>].

[54] G.L. Song, A. Atrens, D. StJohn, An Hydrogen Evolution Method for the Estimation of the Corrosion Rate of Magnesium Alloys, *Magnesium Technology*, (2001) 255-262.
<https://doi.org/10.1002/9781118805497.ch44>.

[55] Y. Jin, C. Blawert, F. Feyerabend, J. Bohlen, M. Silva Campos, S. Gavras, B. Wiese, D. Mei, M. Deng, H. Yang, R. Willumeit-Römer, Time-sequential corrosion behaviour observation of micro-alloyed Mg-0.5Zn-0.2Ca alloy via a quasi-in situ approach, *Corros. Sci.* , 158 (2019) 108096.
<https://doi.org/10.1016/j.corsci.2019.108096>.

[56] N. Wang, R. Wang, C. Peng, B. Peng, Y. Feng, C. Hu, Discharge behaviour of Mg-Al-Pb and Mg-Al-Pb-In alloys as anodes for Mg-air battery, *Electrochim. Acta* 149 (2014) 193-205.

<https://doi.org/10.1016/j.electacta.2014.10.053>.

[57] A.A. Nayeb-Hasheml, J.B. Clark, R.W. Olesinski, G.J. Abbaschian, The Ge-Mg (Germanium-Magnesium) System, *Bulletin of Alloy Phase Diagrams*, 5 (1984).

<https://doi.org/10.1007/BF02872950>.

[58] B. Kim, K. Park, H. Kimura, Y. Park, I. Park, Influence of Addition of Ge on the Microstructure and Corrosion Properties of Magnesium, *Mater. Trans.* , 53 (2012) 240-243.

<https://doi.org/10.2320/matertrans.M2011240>.

[59] D. Bian, W. Zhou, J. Deng, Y. Liu, W. Li, X. Chu, P. Xiu, H. Cai, Y. Kou, B. Jiang, Y. Zheng, Development of magnesium-based biodegradable metals with dietary trace element germanium as orthopaedic implant applications, *Acta Biomater.* , 64 (2017) 421-436.

<https://doi.org/10.1016/j.actbio.2017.10.004>.

[60] I.-H. Jung, J. Kim, Thermodynamic modeling of the Mg-Ge-Si, Mg-Ge-Sn, Mg-Pb-Si and Mg-Pb-Sn systems, *J. Alloys Compd.* , 494 (2010) 137-147.

<https://doi.org/10.1016/j.jallcom.2010.01.045>.

[61] Y. Song, D. Shan, E.-H. Han, Pitting corrosion of a Rare Earth Mg alloy GW93, *Journal of Materials Science & Technology*, 33 (2017) 954-960. <https://doi.org/10.1016/j.jmst.2017.01.014>.

[62] X. Liu, J. Xue, P. Zhang, Z. Wang, Effects of the combinative Ca, Sm and La additions on the electrochemical behaviors and discharge performance of the as-extruded AZ91 anodes for Mg-air batteries, *J. Power Sources* 414 (2019) 174-182. <https://doi.org/10.1016/j.jpowsour.2018.12.092>.

[63] X. Chen, Q. Zou, Q. Le, J. Hou, R. Guo, H. Wang, C. Hu, L. Bao, T. Wang, D. Zhao, F. Yu, A. Atrens, The quasicrystal of Mg-Zn-Y on discharge and electrochemical behaviors as the anode for Mg-air battery, *J. Power Sources* 451 (2020) 227807. <https://doi.org/10.1016/j.jpowsour.2020.227807>.

[64] X. Chen, S. Ning, Q. Le, H. Wang, Q. Zou, R. Guo, J. Hou, Y. Jia, A. Atrens, F. Yu, Effects of external field treatment on the electrochemical behaviors and discharge performance of AZ80 anodes for Mg-air batteries, *Journal of Materials Science & Technology*, 38 (2020) 47-55.

<https://doi.org/10.1016/j.jmst.2019.07.043>.

- [65] Y. Wu, Z. Wang, Y. Liu, G. Li, S. Xie, H. Yu, H. Xiong, AZ61 and AZ61-La Alloys as Anodes for Mg-Air Battery, *J. Mater. Eng. Perform.* , 28 (2019) 2006-2016. <https://doi.org/10.1007/s11665-019-03985-5>.
- [66] N. Shrestha, K.S. Raja, V. Utgikar, Mg-RE Alloy Anode Materials for Mg-Air Battery Application, *J. Electrochem. Soc.* , 166 (2019) A3139-A3153. <https://doi.org/10.1149/2.0131914jes>.
- [67] X. Li, H. Lu, S. Yuan, J. Bai, J. Wang, Y. Cao, Q. Hong, Performance of Mg-9Al-1In Alloy as Anodes for Mg-Air Batteries in 3.5 wt% NaCl Solutions, *J. Electrochem. Soc.* , 164 (2017) A3131-A3137. <https://doi.org/10.1149/2.0971713jes>.
- [68] S. Yuan, H. Lu, Z. Sun, L. Fan, X. Zhu, W. Zhang, Electrochemical Performance of Mg-3Al Modified with Ga, In and Sn as Anodes for Mg-Air Battery, *J. Electrochem. Soc.* , 163 (2016) A1181-A1187. <https://doi.org/10.1149/2.0371607jes>.
- [69] J. Ma, G. Wang, Y. Li, F. Ren, A.A. Volinsky, Electrochemical performance of Mg-air batteries based on AZ series magnesium alloys, *Ionics*, 25 (2018) 2201-2209. <https://doi.org/10.1007/s11581-018-2705-1>.
- [70] N. Birbilis, G. Williams, K. Gusieva, A. Samaniego, M.A. Gibson, H.N. McMurray, Poisoning the corrosion of magnesium, *Electrochem. Commun.* , 34 (2013) 295-298. <https://doi.org/10.1016/j.elecom.2013.07.021>.
- [71] G. Williams, H.A.-L. Dafydd, H.N. McMurray, N. Birbilis, The influence of arsenic alloying on the localised corrosion behaviour of magnesium, *Electrochim. Acta* 219 (2016) 401-411. <https://doi.org/10.1016/j.electacta.2016.10.006>.
- [72] N. Birbilis, T. Cain, J.S. Laird, X. Xia, J.R. Scully, A.E. Hughes, Nuclear Microprobe Analysis for Determination of Element Enrichment Following Magnesium Dissolution, *ECS Electrochemistry Letters*, 4 (2015) C34-C37. <https://doi.org/10.1149/2.0081510eel>.
- [73] T. Cain, S.B. Madden, N. Birbilis, J.R. Scully, Evidence of the Enrichment of Transition Metal Elements on Corroding Mg Surface Using Rutherford Backscattering Spectrometry, *J. Electrochem. Soc.* , 162 (2015) C228-C238. <https://doi.org/10.1149/2.0541506jes>].
- [74] M. Liu, G.-L. Song, Impurity control and corrosion resistance of magnesium-aluminum alloy, *Corros. Sci.* , 77 (2013) 143-150. <https://doi.org/10.1016/j.corosci.2013.07.037>.

[75] J.I. Kim, H.N. Nguyen, B.S. You, Y.M. Kim, Effect of Y addition on removal of Fe impurity from magnesium alloys, *Scr. Mater.* , 162 (2019) 355-360.

<https://doi.org/10.1016/j.scriptamat.2018.11.046>.

[76] G. Ben-Hamu, D. Eliezer, K.S. Shin, The role of Si and Ca on new wrought Mg–Zn–Mn based alloy, *Materials Science and Engineering: A*, 447 (2007) 35-43.

<https://doi.org/10.1016/j.msea.2006.10.059>.

[77] M. Mohedano, B.J.C. Luthringer, B. Mingo, F. Feyerabend, R. Arrabal, P.J. Sanchez-Egido, C. Blawert, R. Willumeit-Römer, M.L. Zheludkevich, E. Matykina, Bioactive plasma electrolytic oxidation coatings on Mg-Ca alloy to control degradation behaviour, *Surf. Coat. Technol.* , 315 (2017) 454-467.

<https://doi.org/10.1016/j.surfcoat.2017.02.050>.

Figures

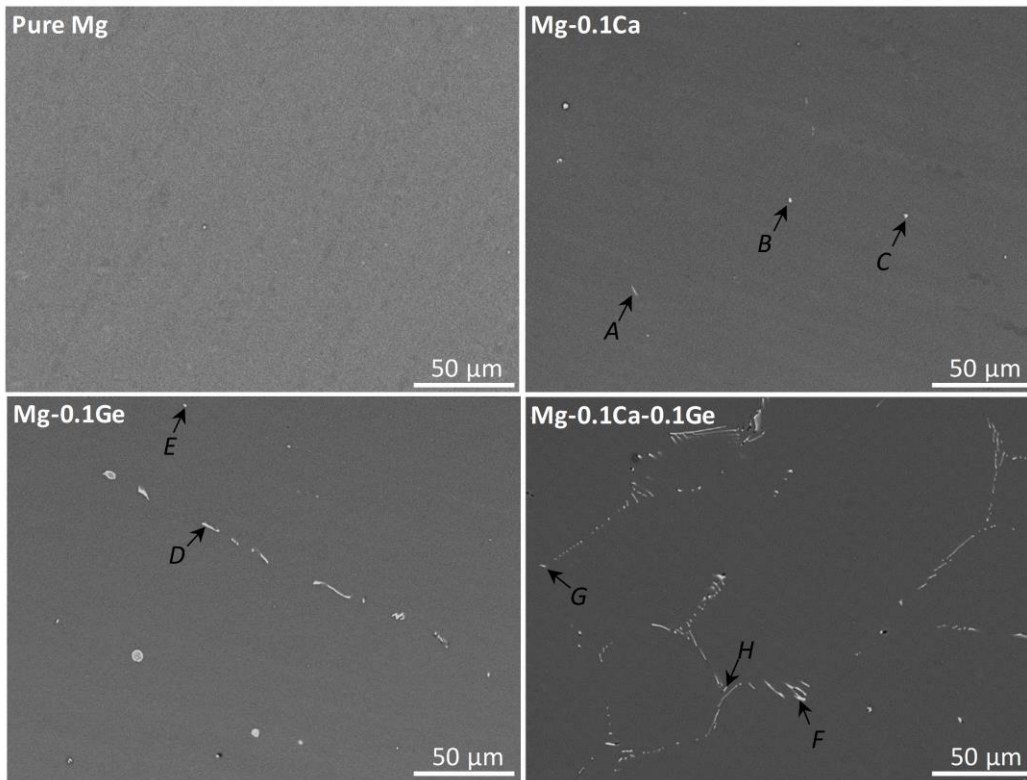


Fig. 1 SEM (BSE) images of as-cast pure Mg and Mg alloys.

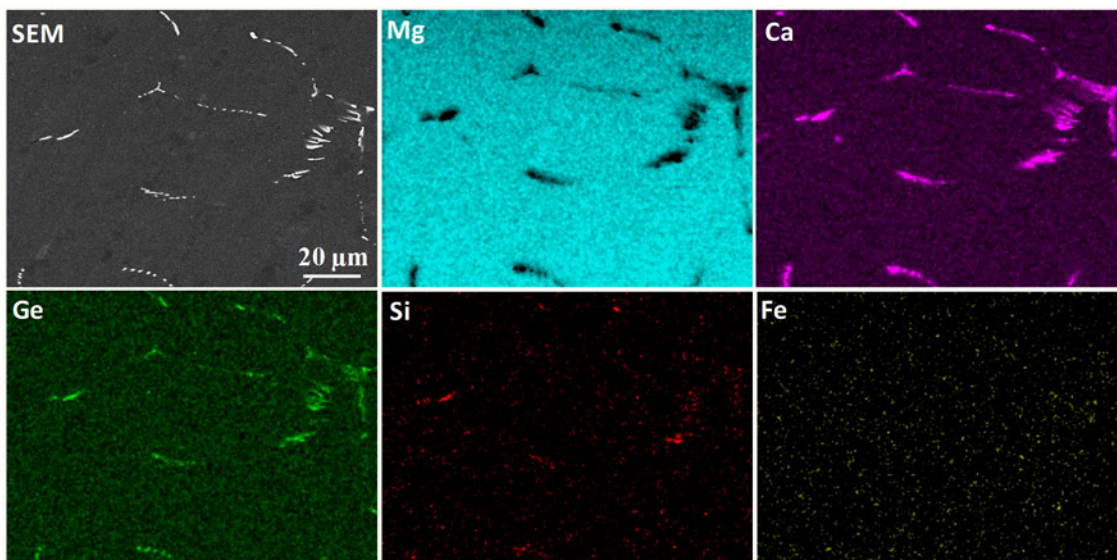


Fig. 2 Elemental mapping for a selected region in Mg-0.1Ca-0.1Ge alloy.

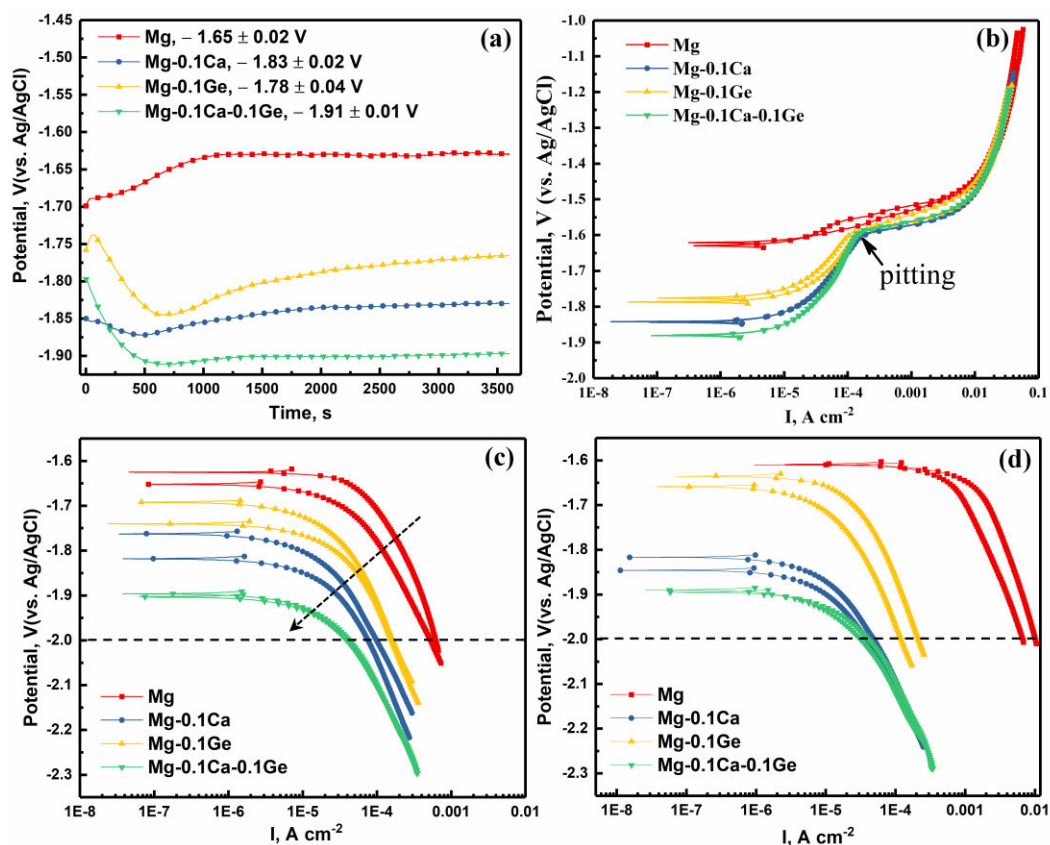


Fig. 3 (a) The evaluation of OCP curves during immersion and calculated average OCP values of three independent measurements. (b) Anodic polarization curves after one-hour OCP measurements. (c) Cathodic polarization curves after one-hour OCP measurements. (d) Cathodic polarization curves after 24-hour immersion. All measurements are performed in unbuffered 3.5 wt% NaCl solution with the initial pH 5.6 ± 0.2 .

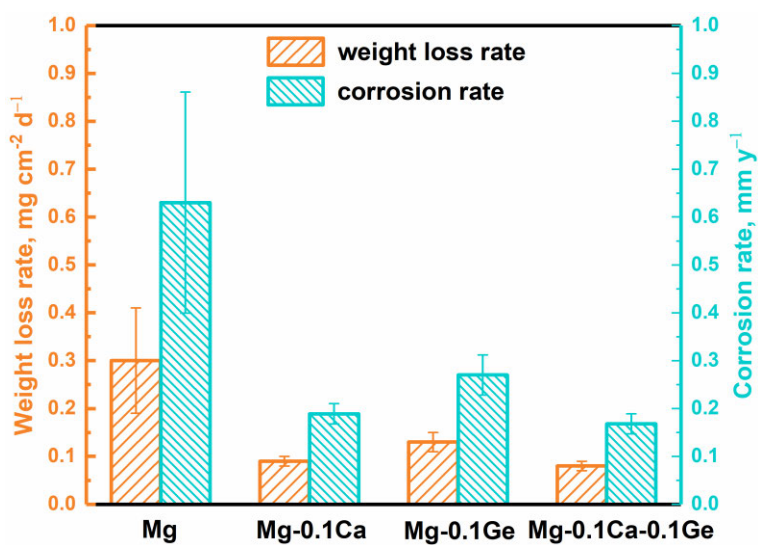


Fig. 4 Weight loss and associated corrosion rates of all studied materials within the 7-day immersion period in 3.5 wt% NaCl solution.

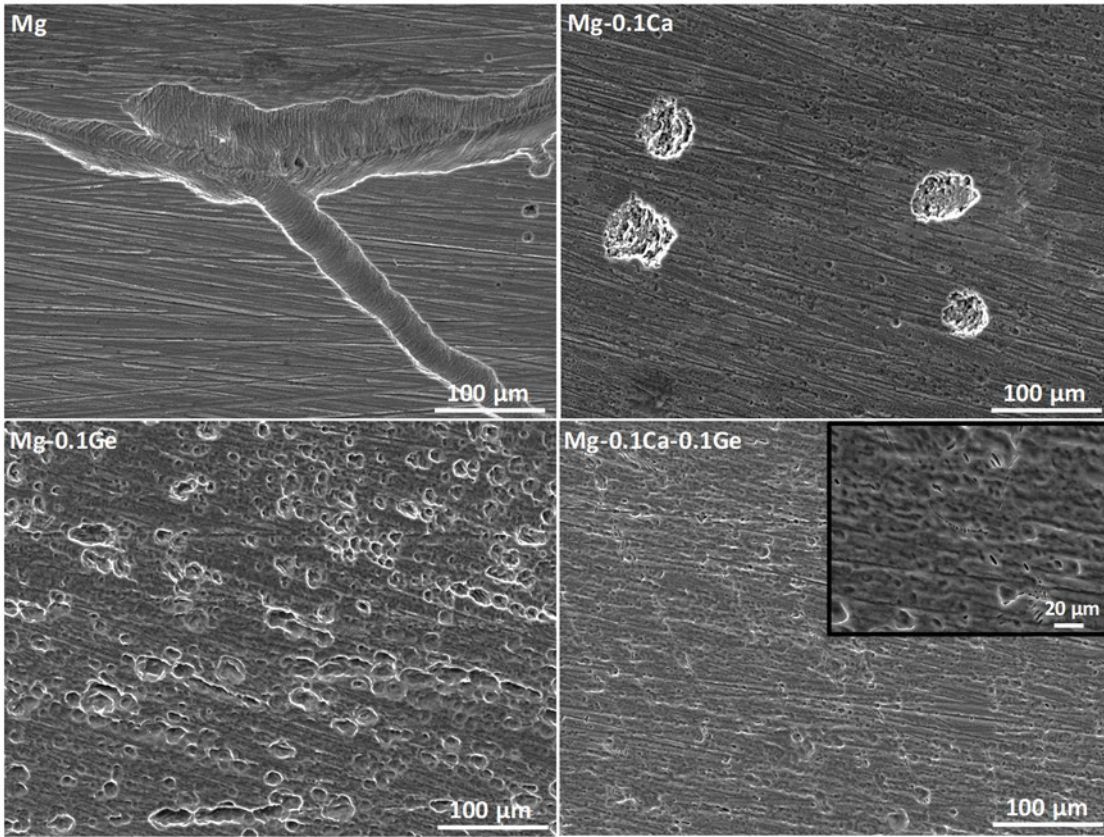


Fig. 5 Surface morphologies of all materials after 7-day immersion tests in 3.5 wt% NaCl solution and cleaning with chromic acid to remove corrosion products.

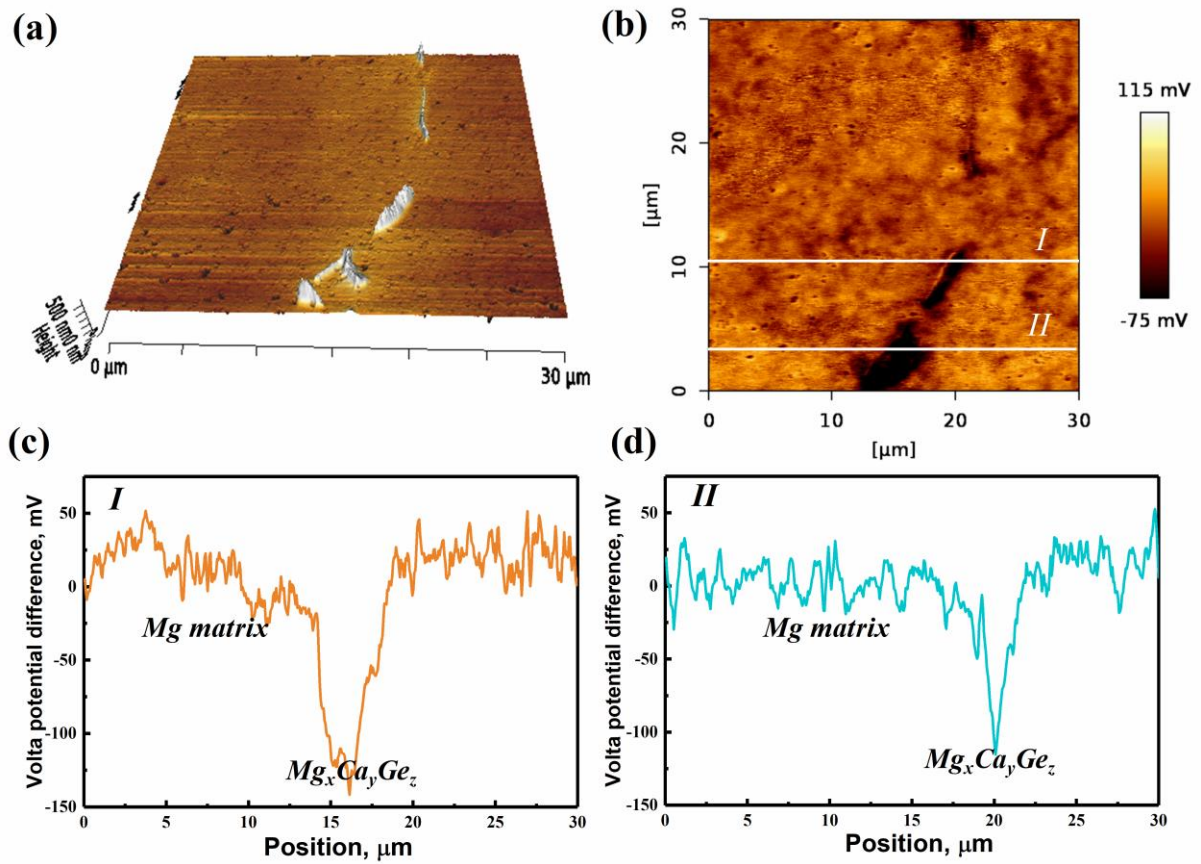


Fig. 6 SKPFM analysis of Mg-0.1Ca-0.1Ge alloy: (a) 3D height map; (b) corresponding Volta potential map; (c, d) corresponding line profile along line I and II marked in (b).

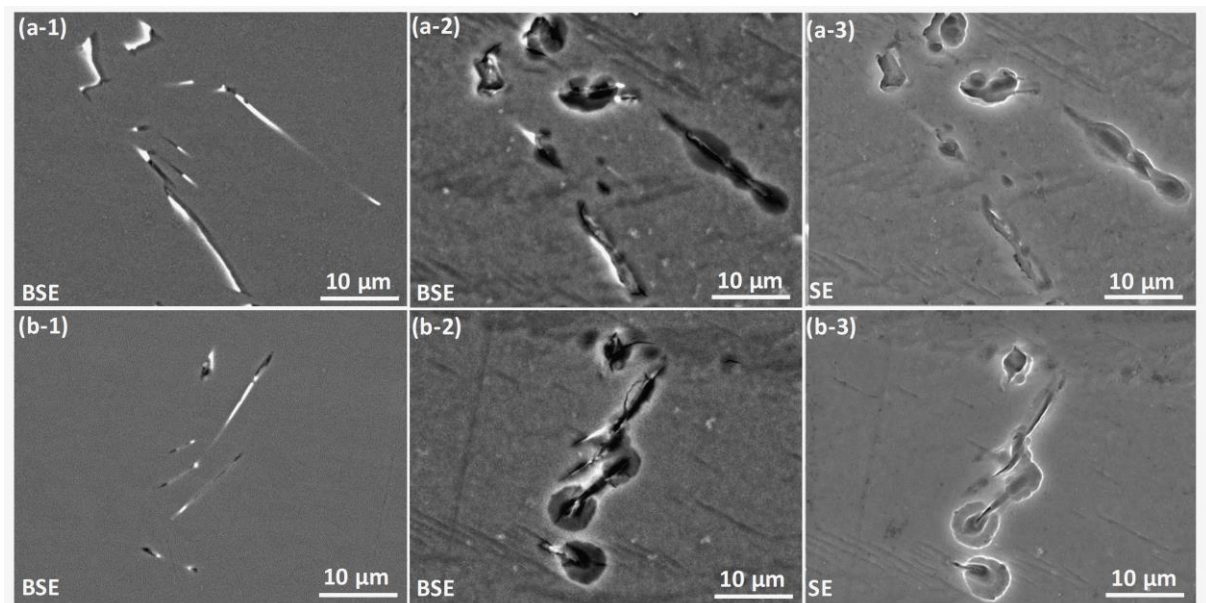


Fig. 7 (a-1, b-1) Morphologies of marked regions in Mg-0.1Ca-0.1Ge alloy before immersion. (a-2, b-2) Morphologies of the same regions after immersion for 10 min in 3.5 wt% NaCl solution. (a-3, b-3) Morphologies of the same regions after removing corrosion products with chromic acid.

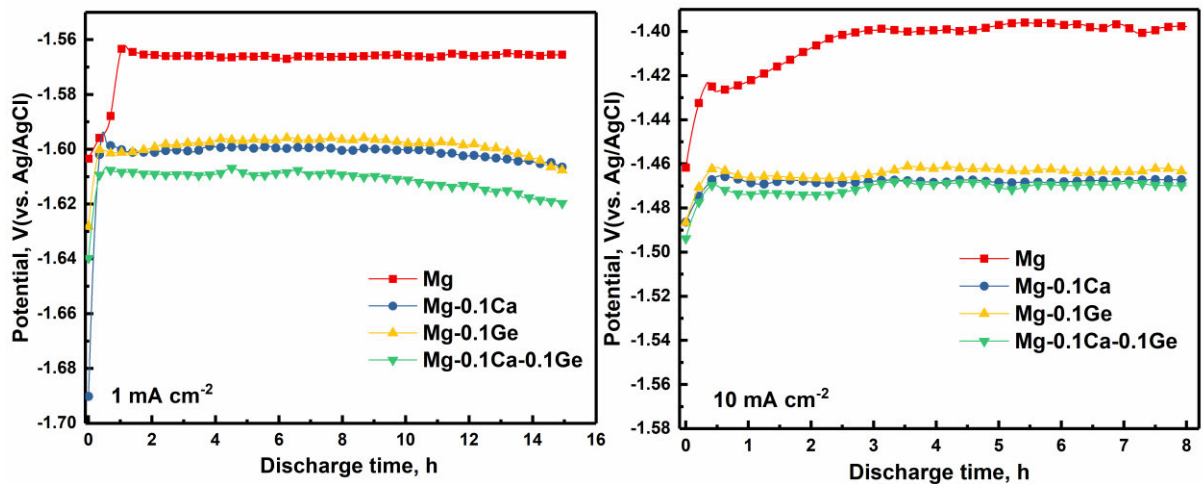


Fig. 8 Discharge curves of all cast Mg anodes at different current densities in 3.5 wt% NaCl solution.

Typical results of replicated measurements are presented.

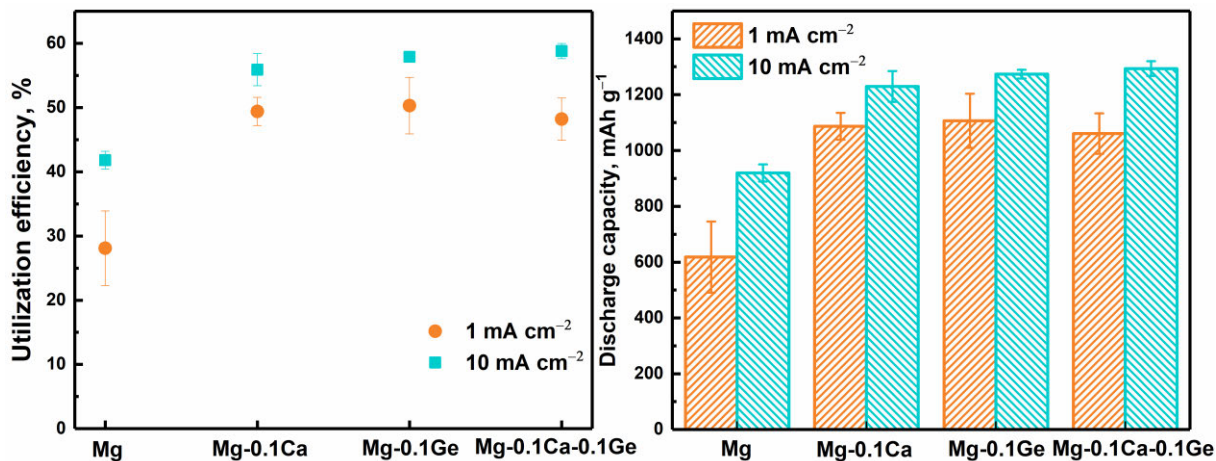


Fig. 9 Utilization efficiency and discharge capacity of Mg anodes under different discharge current densities in 3.5 wt% NaCl solution.

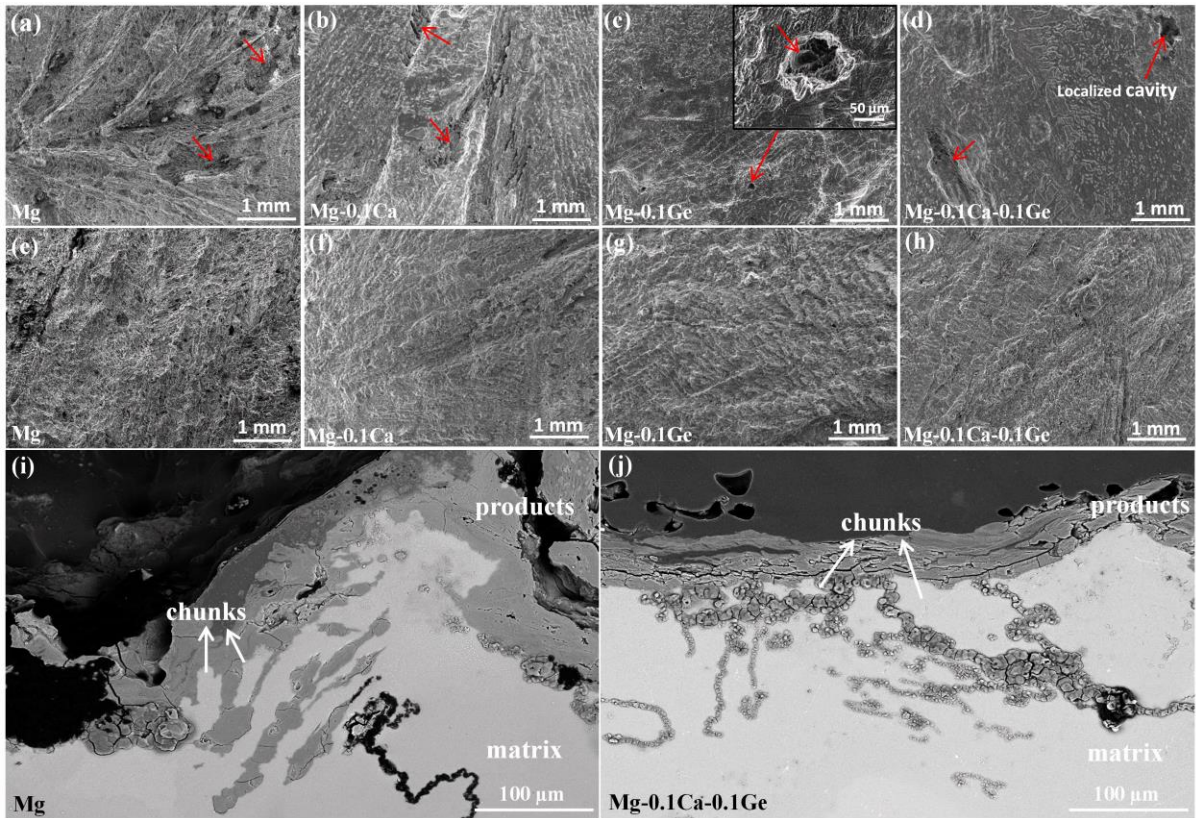


Fig. 10 Surface morphologies of different Mg anodes after discharge and removal of discharge products: (a-d) 1 mA cm^{-2} for 15 h, (e-h) 10 mA cm^{-2} for 8 h. The cross-sectional morphologies of recast pure Mg and Mg-0.1Ca-0.1Ge after discharge at 1 mA cm^{-2} are shown in (i) and (j), respectively.

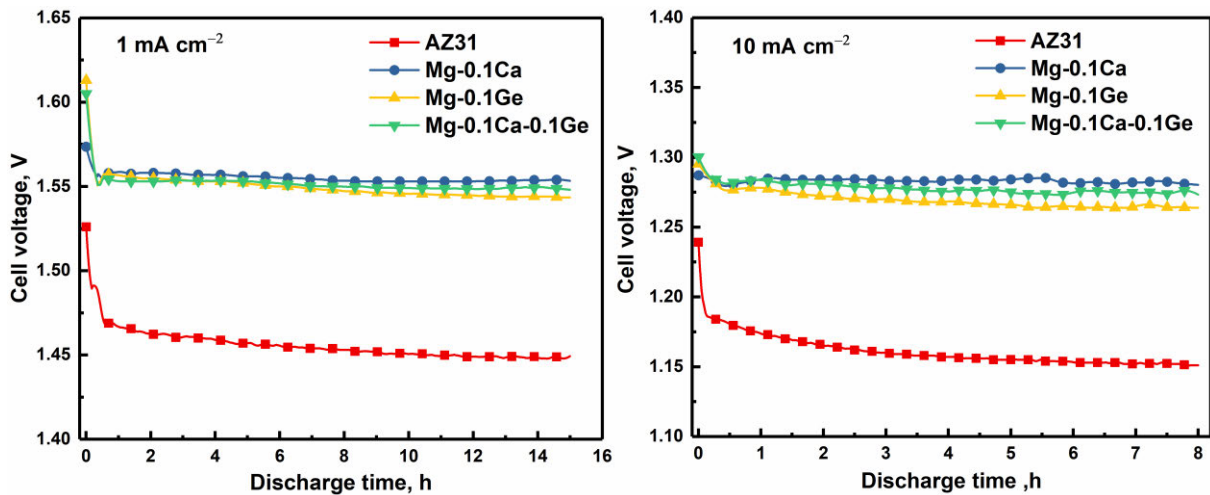


Fig. 11 Discharge curves of a custom-made Mg-air full cell adopting different anodes operated at two current densities. The electrolyte is 3.5 wt% NaCl solution (unbuffered, pH 5.6). The catalyst utilized in the commercially air cathode is C/MnO₂ mixture.

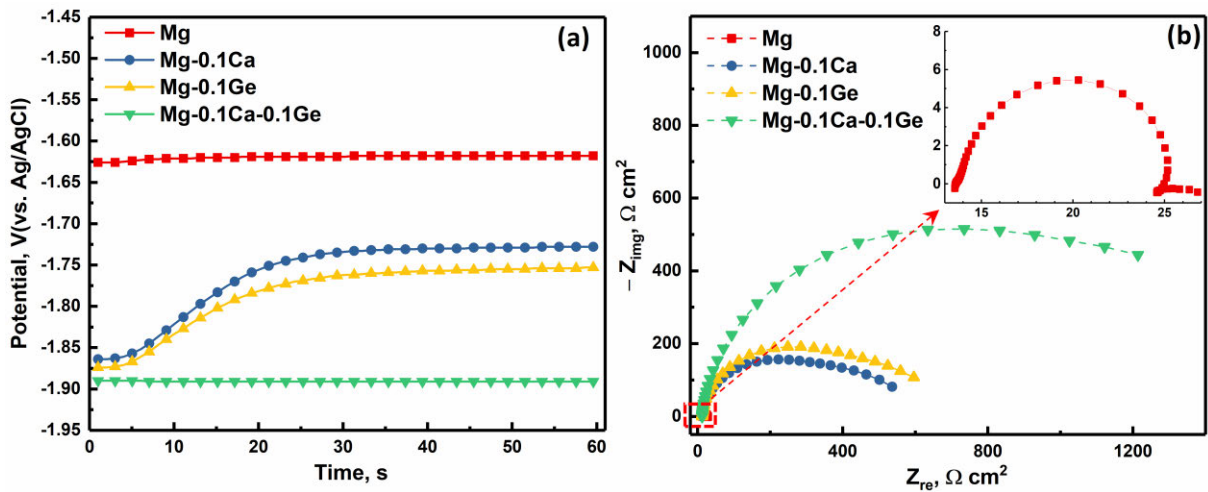


Fig. 12 (a) OCP- time curves and (b) EIS Nyquist plots of all materials measured after discharge at 10 mA cm^{-2} for 0.5 hour.

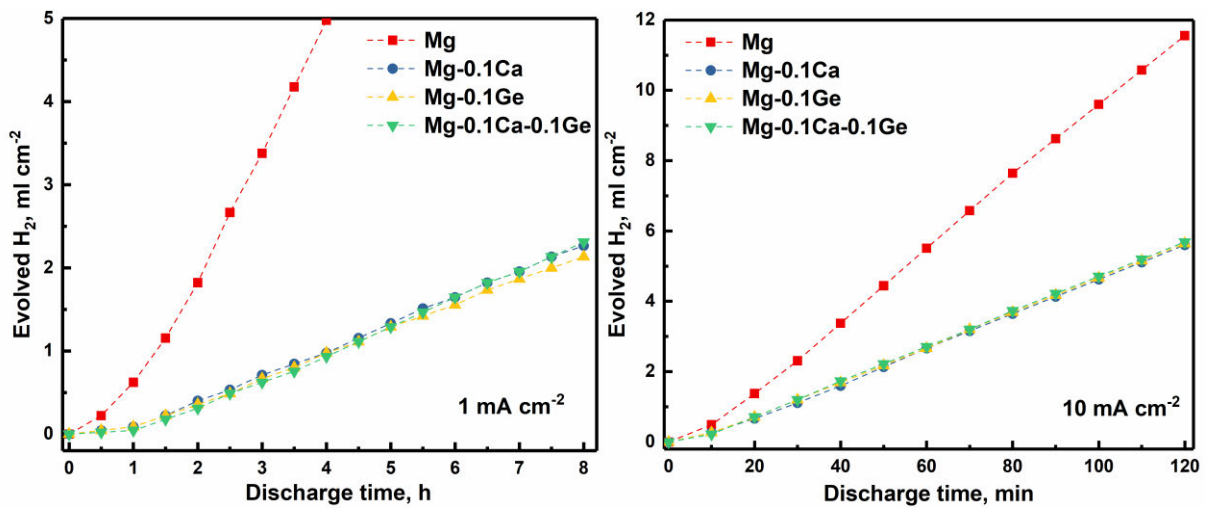


Fig. 13 Real-time hydrogen evolution determined during discharge at different current densities in 3.5 wt% NaCl solution. Representative results of triplicated measurements are presented.

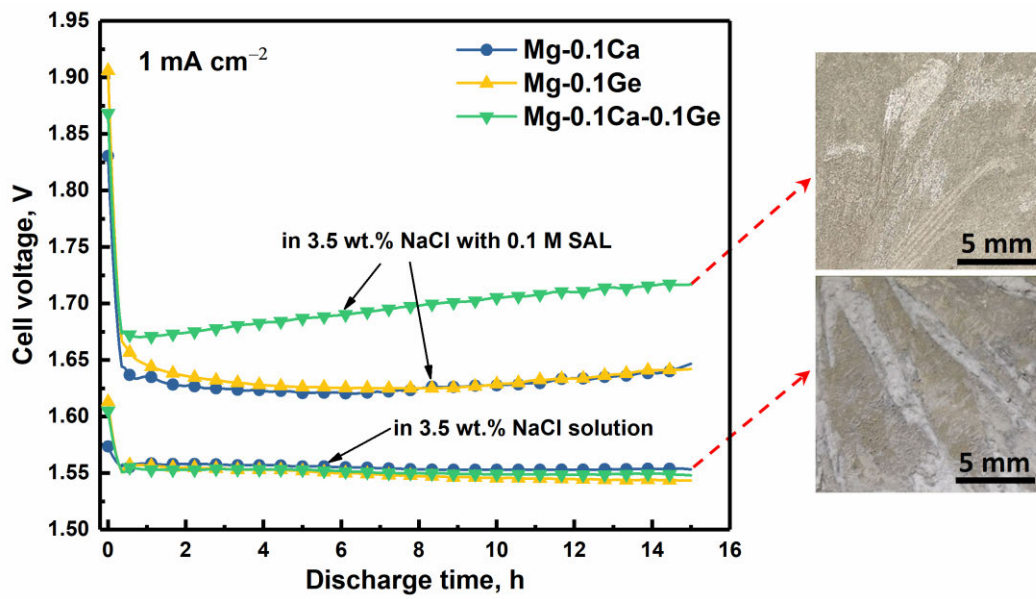


Fig. 14 Voltage profile of the custom-made Mg-air full cell adopting different anodes at 1 mA cm^{-2} in the electrolyte with an additive, i.e. 0.1 M salicylate (SAL, initial pH adjusted to 7). Data in blank NaCl solution extracted from Fig. 11 are included for comparison. Optical images of anode surface after discharge is also presented.